

Spin-dependent Transport Studies of Fe/Mo_xCr_{1-x}S₂/Fe Magnetic Tunnel Junction

Aloka Ranjan Sahoo^{1,2} and Sharat Chandra^{1,2}

¹Materials Science Group, Indira Gandhi Centre for Atomic Research, Kalpakkam, 603102, Tamil Nadu, India

²Homi Bhabha National Institute, Mumbai, 400094, India

Corresponding author's email: alokranjanctc@gmail.com, sharat@igcar.gov.in

Keywords: Heterostructure, Interface, Density functional theory, Spin transport, Molybdenum disulfide

Abstract

Using Density functional theory and non-equilibrium Green's function formalism, spin-dependent electron transport in Fe/Mo_xCr_{1-x}S₂/Fe magnetic tunnel junction is studied. Spin-transport for different thicknesses (1, 3, 5, and 7 layers) of the spacer MoS₂ and for two different surface orientations of the Fe electrode, the Fe(001) and Fe(111) surface and the effect of substitutional doping of magnetic impurity Cr on the spin-transport of the junctions is investigated. The electronic structure of the heterostructure shows presence of metal-induced states in the semiconducting MoS₂ at the Fe/MoS₂ interface and the effect of the interface is limited to the first two layers of MoS₂ from the interface. The I-V characteristics of the junctions for the monolayer and three-layer MoS₂ spacer show linear behaviour due to the metallic nature of the junction. The tunneling nature of the junction is observed for the thicker junctions with five-layer and seven-layer spacers. With the introduction of magnetic impurity, we have shown that spin-polarisation in the spacer is improved, thus increasing the spin-polarised current. The Cr-defect states are observed below the conduction band and the Cr-doped devices are stable up to a bias of 0.5V. The close packed Fe(111) surface is better electrode material for tunneling of electrons through the junction compared to the Fe(001) surface due to lower surface energy and reduced transmission.

INTRODUCTION

A typical spin electronic device, magnetic tunnel junctions (MTJ), is a bi-stable device consisting of a stacked thin, insulating, non-magnetic barrier layer of nm thickness sandwiched between two ferromagnetic electrodes. The resistance of the MTJ can be varied by changing the relative orientation of the magnetisation of the ferromagnetic electrode layers [1,2]. The ferromagnetic electrodes act as a polariser and an analyser of the spin information carried by the current, and the normalised difference between the resistance obtained in these two configuration states is defined as tunnelling magnetoresistance (TMR). The observation of giant magnetoresistance (GMR) in spin-dependent transport in metallic multi-layer [3] and the fundamentals of the tunnel magneto resistive (TMR) and GMR effects lead to the enhancement of thousands of times more memory storage capacity [4].

Spintronics devices use both charge and spin degrees of freedom of an electron for the transport and storage of information. Efficient data processing with electron transport and storage of information through an assembly of spin requires generation, injection and detection of spin-polarised current in a spintronics device [5–7]. Compared to traditional microelectronic devices, spintronics devices function more quickly and generate less heat since switching a spin state requires less energy than controlling and manipulating a charge current [8]. Potential applications of spintronics include precision sensors, new power-efficient integration architectures, and spin-based fast and ultra-low-power non-volatile devices such as the new spin-transfer-torque magnetic random-access memory (MRAM) [9,10], widely distributed applications in data storage [11]. This is the demand of Modern Electronics, seeking high-speed data transfer and low-power dissipation. Spintronics aims to

provide more complex architectures and a robust solution beyond CMOS [5,12]. Current silicon complementary metal-oxide-semiconductor devices that rely on charge manipulation are most likely to be replaced by devices that manipulate spin.

Traditional MTJ prepared with wide band gap oxide spacers lacks control over layer thickness and smooth surface. Understanding the proximity effects of hybridisation at the interface between ferromagnetic metal and spacer layer is difficult with conventional oxide-based magnetic tunnel junction due to poor crystalline and the absence of a smooth interface. In contrast, two-dimensional (2D) materials with atomically thin crystals, free of dangling bonds and control over layer thickness, can be grown on a ferromagnetic electrode layer to provide high-quality, smooth interfaces [13]. The successful demonstration of isolation of single atomic layer thickness graphene from its bulk counterpart graphite and the remarkable properties arising from the confinement of electron transport into a plane leads to growing interest in exploring other 2D materials of atomic thickness beyond graphene [14–18]. Spintronics based on 2D materials has received much attention because of the prominent mechanical, optical, electrical, and magnetic properties of 2D materials [14,19–22]. The carbon atoms arranged in a honeycomb 2D lattice in Graphene show unique linearly dispersive Dirac band structure and electron-hole symmetry [14,19,20,23,24] and high mobility of charge carriers [14,25,26]. The long spin lifetimes and diffusion lengths [27–31] and gate-tunable carrier concentration [19,32] in graphene are particularly attractive for spintronics applications [33–36].

The zero band gap and weak spin-orbit coupling (SOC) in graphene make it challenging to build graphene-based current switches and spintronics applications. In contrast

to this, the monolayer MoS₂ offers quite distinct properties like a high current on-off switching rate (10⁸), high carrier mobility (~200 cm²/Vs), high thermal stability and ultralow standby power dissipation have been demonstrated in the field effect transistor [37], tunable band gap, quantum spin Hall effect [38], optical and photocatalytic properties [39]. In addition, MoS₂ and other transition metal dichalcogenides (TMDs) are known to have strong SOC [40–42]. The valley polarisation in MoS₂ provides a platform for encoding information [43–45] and allows manipulation of the spin and valley degrees of freedom [43,46–49]. These 2D materials are very attractive for spintronics, which aims to utilise the spin degree freedom of electrons for novel information storage and logic devices [5,7,50,51]. The transition metal dichalcogenide (TMDs) MoS₂ has a layered structure with Mo sandwiched between two hexagonal planes of S in a trigonal prismatic arrangement. The intra-layer bonding of S-Mo-S is covalent, and inter-layer S-Mo-S sandwiches interact via weak van der Waals force [52,53]. The indirect band gap of 1.2 eV in bulk MoS₂ changes to the direct band gap of 1.8 eV in monolayer MoS₂ [54,55]. The tunability of the band gap, ultra-thin layered structure, and high carrier mobility make it a suitable candidate for 2D material-based device application [56–58].

Oxide-based wide band gap MgO and Al₂O₃ serving as a 2D spacer in MTJ has been proposed, and it does not give the desired high magnetoresistance (MR) in vertical Spin valves [59–62]. Efficient spin injection and giant magnetoresistance (GMR) using MoS₂ as a spacer and Fe (001) as a ferromagnetic electrode have been reported by K. Dolui *et al.* [56]. They have studied using Fe(001) as an electrode and applied a strain of 10% on Fe to match

the lattice of MoS₂. Khaldoun *et al.* reported considerable magneto resistance in planar Fe/MoS₂ junction using MoS₂ Nano ribbon [63]. Experimentally, Han-Chun demonstrated a large transverse magnetoresistance at the Fe₃O₄/MoS₂/Fe₃O₄ junction. They observed a clear tunnelling magnetoresistance (TMR) signal below 200 K [57]. Recently, Worsak et al. used Fe₃Si Heusler alloy as an electrode for MoS₂-based magnetic tunnel junction [64]. NiFe/MoS₂ interface has also been investigated, and the spin-valve effect is observed up to 240 K, with the highest magnetoresistance (MR) up to 0.73% at low temperatures [58], and also from the first-principle electron transport calculations, which reveal MR of ~9% for an ideal Py/MoS₂/Py junction. DFT calculation for the electronic structure of interfaces with Fe/MoS₂ Co/MoS₂ and Fe₃O₄/MoS₂ has been studied with different surfaces of ferromagnetic material with MoS₂(001) surface [65].

Interfaces play a crucial role in the spin-polarised transport across the ferromagnetic-semiconductor interfaces and are distinct to the individual materials forming the junction. The efficiency of injecting or detecting spin-polarised electrons across such an interface depends on several features, such as interface roughness, defects, impurities, and mismatch in conductivity of the materials forming the interface [66]. The proximity effect of the ferromagnet on the band structure of the semiconducting spacer results in spin-selective transmission. Thus, the tunneling spin-polarisation is not an intrinsic property of the ferromagnetic electrode alone but depends on the crystalline structure and electronic properties of the insulator and the ferromagnetic/insulator interfaces [67,68]. Understanding the electronic structure of heterostructures is essential in studying their transport properties. The Fe(111) surface has low surface energy, is densely packed and is the most stable surface,

has a hexagonal symmetry the same as MoS₂, thus creating a low lattice mismatch interface. In the present work, the layer-dependent electronic structure and spin transport in Fe/MoS₂/Fe junctions with different ferromagnetic electrode Fe surface Fe(001) and Fe(111), the effect of magnetic impurity Cr-doped MoS₂ layers on the spin-transport properties of the junction and the I-V characteristics of the junctions are studied.

Computational Details

The spin-dependent electron transport studies for Fe/MoS₂/Fe interfaces are carried out by combining Non-equilibrium Green's function formalism (NEGF) and the density functional theory (DFT) as implemented in the QuantumATK package [69–71]. We have used local density approximation (LDA) exchange-correlation potential to describe the exchange-correlation effect [72]. The LCAO double-zeta polarised basis set is used for all the elements with a density mesh cut-off of 150 Hartree [73,74]. We have used *bcc* Fe and hexagonal MoS₂ with space group P6₃/mmc for bulk calculations and heterostructure construction. The relaxed optimised lattice parameters for Fe and MoS₂ with LDA exchange-correlation functional is 2.77 Å and 3.14 Å, respectively. For the Fe(001)/MoS₂(001)/Fe(001) junction, the Fe/MoS₂ interface is made by choosing a suitable unit cell and applying strain on both Fe and MoS₂; the applied strain along the planner direction is 4.88% and -2.3% respectively with a mean absolute lattice mismatch of 2.39% [75]. The interface geometry's resulting rectangular in-plane lattice parameters are 2.947 Å and 5.495 Å, respectively. The applied strain along the in-plane lattice direction is relaxed by allowing the interface to relax along the *z*-direction. The heterostructure has six, ten and fourteen units of MoS₂ in the three-, five-, and seven-layer device respectively. For study of spin transport in Cr-doped MoS₂, one

Cr atom is substitutionally doped at the Mo site in the middle layer of three-, five- and seven-layer MoS₂ spacer. The Brillouin zone of Fe(001)/MoS₂/Fe(001) junction is sampled by a K-point mesh of 13×7×153 using Monkhorst-pack scheme [76]. For transmission spectrum calculation, the 2D Brillouin zone is sampled by 109×59 K-points. The Fe(111)/MoS₂ interface geometries are made by taking a Fe(111) surface and placing that MoS₂(001) surface on top of it. The suitable unit cell for interface geometry was then decided by considering the lattice mismatch for different possible unit cells. Final interface geometries were made by applying strain on Fe to match the in-plane lattice parameter of MoS₂, the applied strain on Fe is 6%. The final geometries of Fe(111)/MoS₂(001)/Fe(111) heterostructure where the spacer MoS₂ has a thickness of one layer, three layers and five layers are modelled having in-plane lattice parameters of a=b= 8.319 Å and angle between in-plane lattice vectors is 60 degree. The Brillouin zone is sampled by a Monkhorst-pack with a grid of 5×5×1, and a tolerance of 10⁻⁶ was set for achieving the self-consistency of electronic energy minimisation. For transmission spectrum analysis, the 2D Brillouin zone is ample by 51×51 K-points. In all the heterostructure geometries, we have included a sufficient number of Fe layers to use the model for MTJ device calculation to study electron spin-dependent transport through the Fe(001)/MoS₂(001)/Fe(001) and Fe(111)/MoS₂(001)/Fe(111) sandwich, where it needs to have sufficient number of electrode layers to screen any perturbation due to any scattering by MoS₂ to reach the electrode layers. The applied strain on Fe while making the interface is relaxed first by allowing it to relax along the z-direction. During relaxing the Fe(111)/MoS₂(001)/Fe(111) sandwich, electrode layers are rigidly relaxed as they are bulk-like, and other atoms are completely relaxed to the target force tolerance of 0.02 eV/Å. In the relaxed geometry, the Fe-S bond distance is found to vary from 2.1Å to 2.29Å, which agrees with the experimental Fe-S bond distance of 2.29 Å.

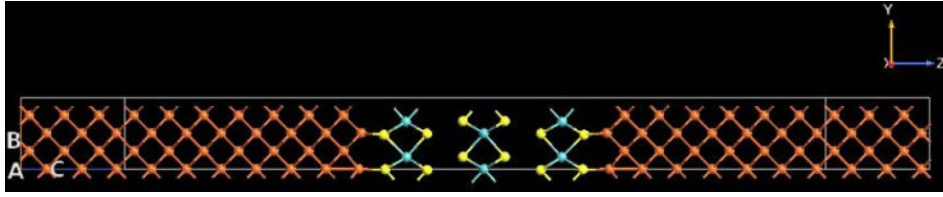


Figure 1 Device geometry for transport in $Fe(001)/MoS_2/Fe(001)$ junction

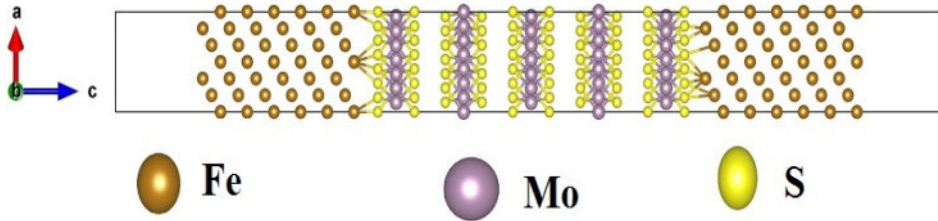


Figure 2 Interface geometry for transport in $Fe(111)/MoS_2/Fe(111)$ interface

Results and Discussions

Spin transport in $Fe(001)/MoS_2/Fe(001)$ Junction

$Fe(001)/MoS_2(3\text{-layer})/Fe(001)$ junction

The total device density of states (DDOS) and projected density of states (PDOS) for the Fe electrodes in the three-layer device is shown in Figure 3(a) and Figure 3(b) respectively. The PDOS for the electrode in Figure 3(b) resembles DOS for bulk Fe.

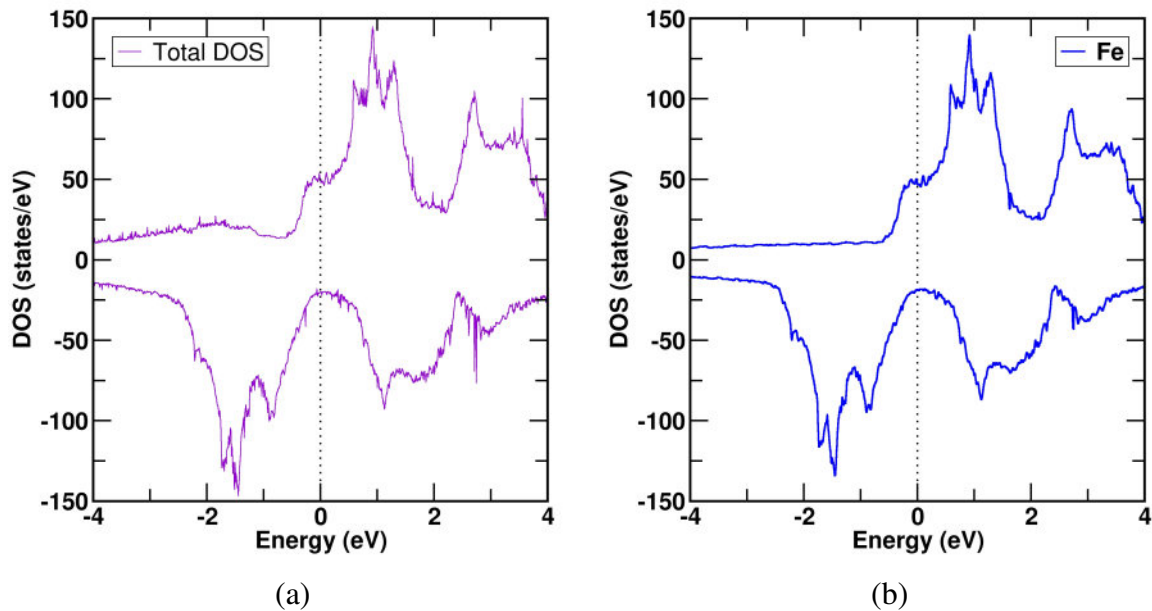


Figure 3 Total Device DOS (a) and PDOS for Fe (b) in $Fe(001)/MoS_2(3\text{-layer})/Fe(001)$ junction.

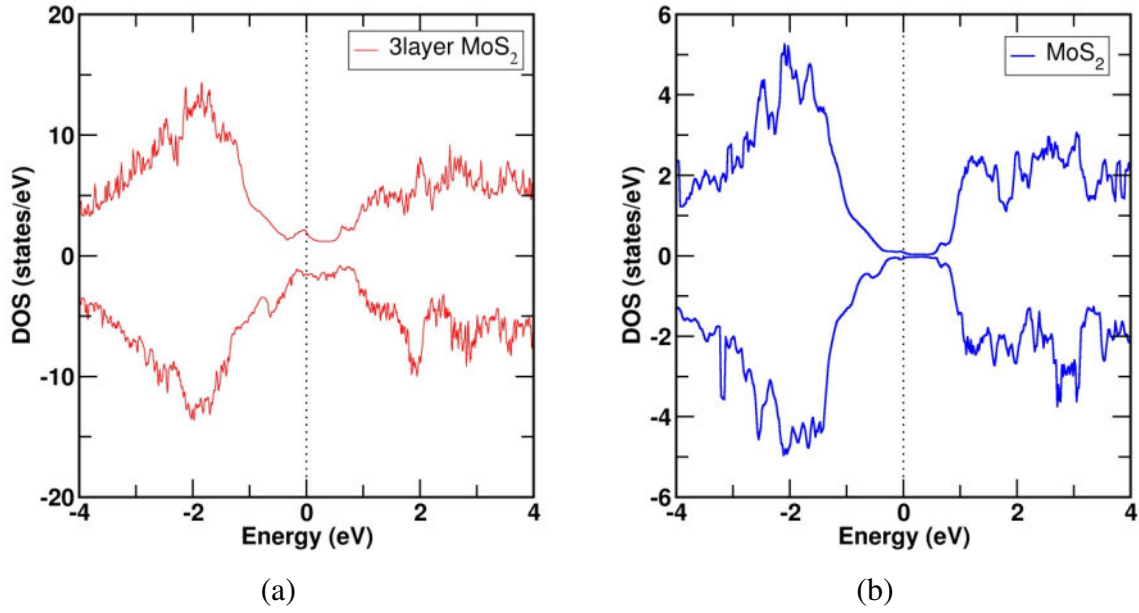


Figure 4 PDOS for three-layer MoS_2 (a) and middle layer MoS_2 (b) in $\text{Fe}(001)/\text{MoS}_2(3\text{-layer})/\text{Fe}(001)$ junction.

The PDOS for three-layer and middle layer (one-layer thickness) MoS_2 in Figure 4 shows that the semiconducting nature of MoS_2 has disappeared after making an interface with the ferromagnetic Fe electrode and the three layer MoS_2 spacer has become metallic. A small spin-polarisation is induced in MoS_2 after forming an interface with Fe layers.

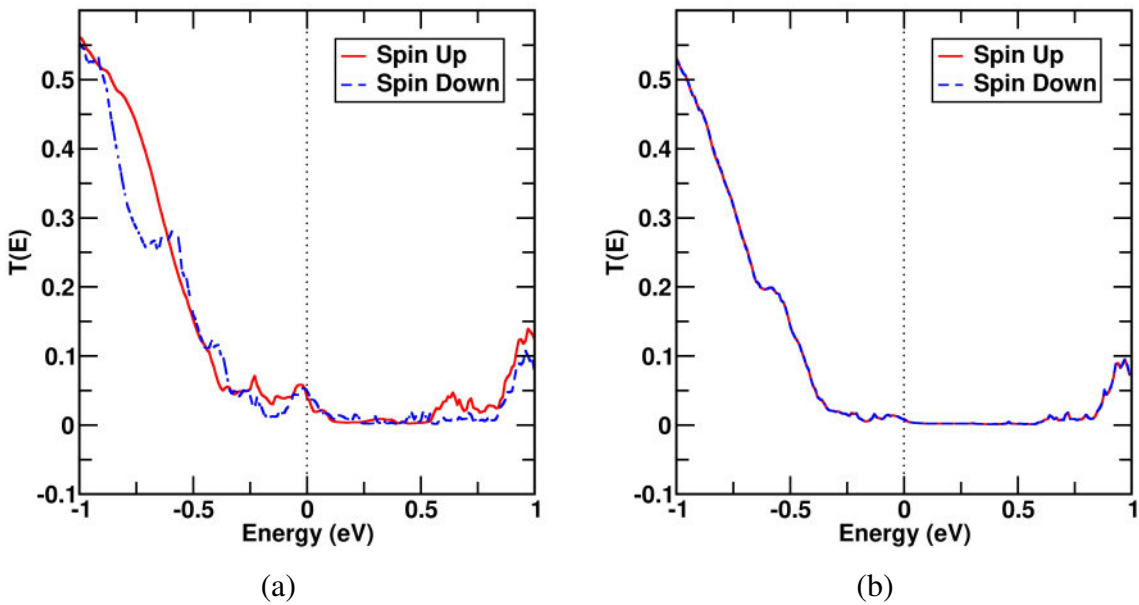


Figure 5 Transmission spectrum for $\text{Fe}(001)/\text{MoS}_2(3\text{-layer})/\text{Fe}(001)$ junction in parallel (a) and anti-parallel (b) orientation of electrodes.

The metallic nature of the junction leads to the finite transmission through the junction under zero-bias conditions, as shown in the transmission spectrum for parallel orientation of the electrodes (P) in Figure 5(a). The spin-up channel has 0.04 transmission at the Fermi level, and the spin-down channel has 0.05 transmission at zero-bias. For the anti-parallel orientation of the electrodes (AP), the junction has 0.008 transmissions for both spin-up and spin-down channels at the Fermi level in zero-bias conditions, as shown in Figure 5(b).

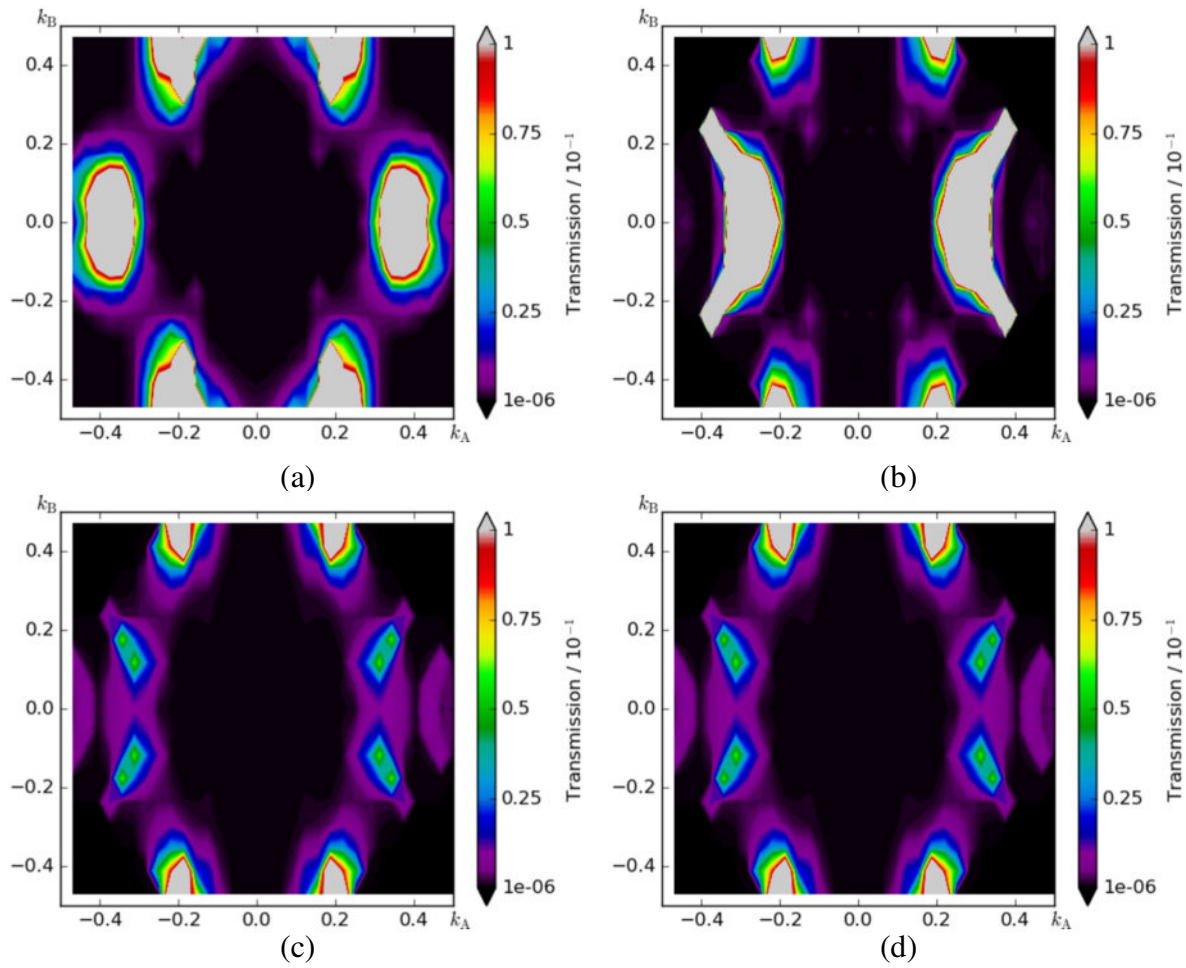


Figure 6 *K*-resolved transmission spectrum in spin-up (left panel) and spin-down (right panel) channel for Fe(001)/MoS₂(3-layer)/Fe(001) junction in parallel (figure a, and b) and anti-parallel (figure c, and d) orientation of electrodes.

The K-resolved transmission spectrum for P and AP is shown in Figure 6. The contribution from the 2D Brillouin zone to the transmission spectrum at each energy is shown with a 2D colour map. The brighter red dots show a higher transmission coefficient,

indicating a higher contribution from the K-point at a particular energy, and a dark dot shows a low transmission coefficient from the K-point at a specific energy, indicating a low contribution from the K-point. The K-resolved transmission spectrum for parallel orientation of the electrodes at Fermi-level under zero-bias condition shows contribution to the transmission coming from the spin-up and spin-down channels. The contribution to the transmission comes from six pockets away from the Brillouin zone centre in the spin-up channel, and for spin-down, two pockets majorly contribute to the transmission. For the anti-parallel orientation of the electrodes, the K-resolved transmission for both the spin channels is identical, as seen from the transmission spectrum in Figure 6 (c) and (d).

The projected local density of states (PLDOS) for the junction with three-layer MoS₂ is shown in Figure 7, In which the DOS of the device is projected over the spatial region of the device along the transport direction, which is z -direction. The transport direction z is sliced into different regions, and the variation of electronic states with respect to the z -direction is shown in the PLDOS. The spatially resolved density of states is shown in the PLDOS with a 2D colour map showing the distribution of electronic states over both energy and real space. Scanning across z -direction shows the change in local electronic structure across the electrode, interface and central scattering region. Brighter red dots show a high presence of states, and a dark/blue dot shows a low presence of states in the energy range and the atomic layer contributing to the DOS. A dark black region shows the absence of states, indicating a band gap for the semiconductor or insulator spacer in the device. The metal-induced states in the semiconductor MoS₂ are observed from the PLDOS of the device with a three-layer MoS₂ spacer. Metal-induced states are present in all three layers of MoS₂, with the first layer of MoS₂ next to Fe layers forming the interface having higher metal-induced states.

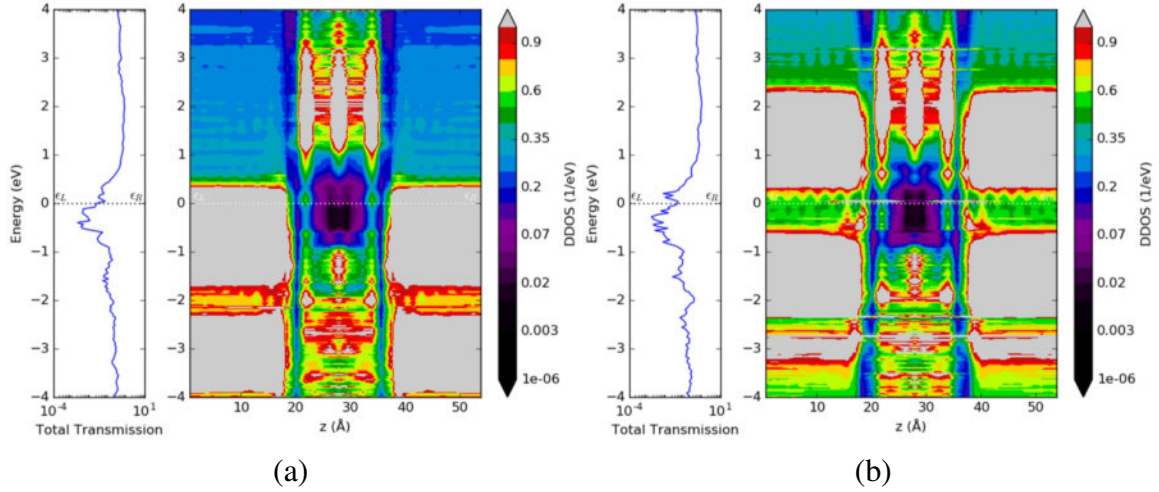


Figure 7 PLDOS for spin-up (a) and spin-down (b) channel in Fe(001)/MoS₂(3-layer)/Fe(001) junction in parallel orientation of electrodes.

With Cr doped in the middle layer of the three-layer MoS₂ in Fe/Mo_xCr_{1-x}S₂(3-layer)/Fe junction, the transmission for both spin-up and spin-down channels in the parallel orientation of the electrodes is 0.025 and in the anti-parallel orientation of electrodes, the transmission is 0.004 for each channel, as shown in Figure 8(a) and (b) respectively.

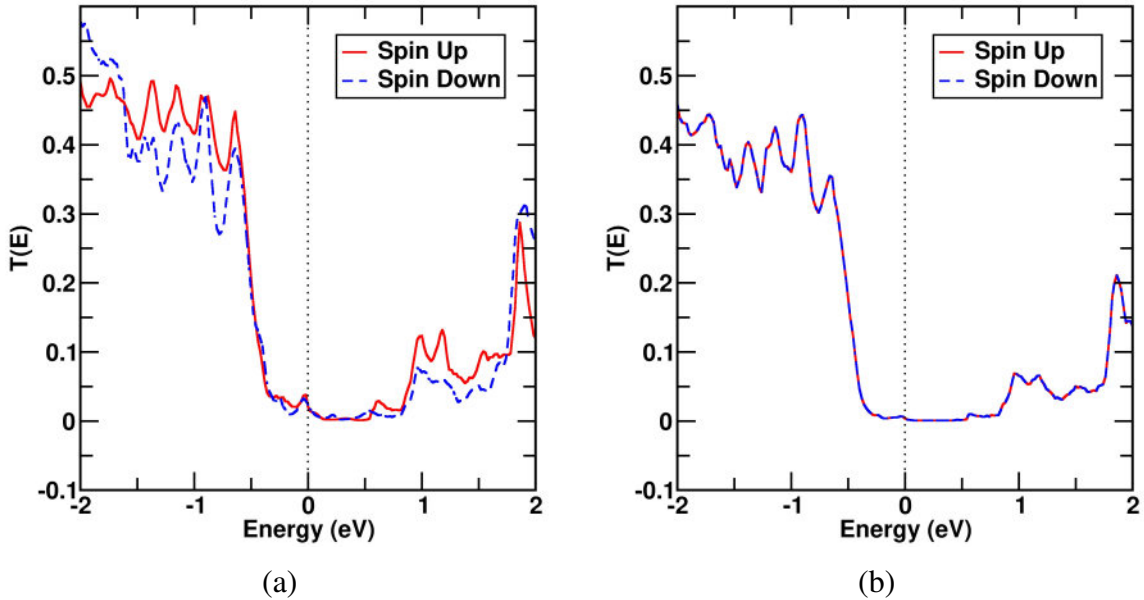


Figure 8 Transmission spectrum for Fe(001)/Mo_xCr_{1-x}S₂(3-layer)/Fe(001) junction in parallel (a) and anti-parallel (b) orientation of electrodes.

The K-resolved transmission spectrum for the P orientation of electrodes in Figure 9 (a) and (b) shows contributions to the transmission from the six pockets of the hexagonal 2D

Brillouin zone in spin-up and spin-down channels. For AP orientation of electrodes, the K -resolved transmission spectrum in Figure 9 (c) and (d) shows that the transmission coefficient is the same for the spin-up and spin-down channels and gets negligible contributions from the 2D Brillouin zone, as seen in the total transmission at zero-bias in Figure 8(b).

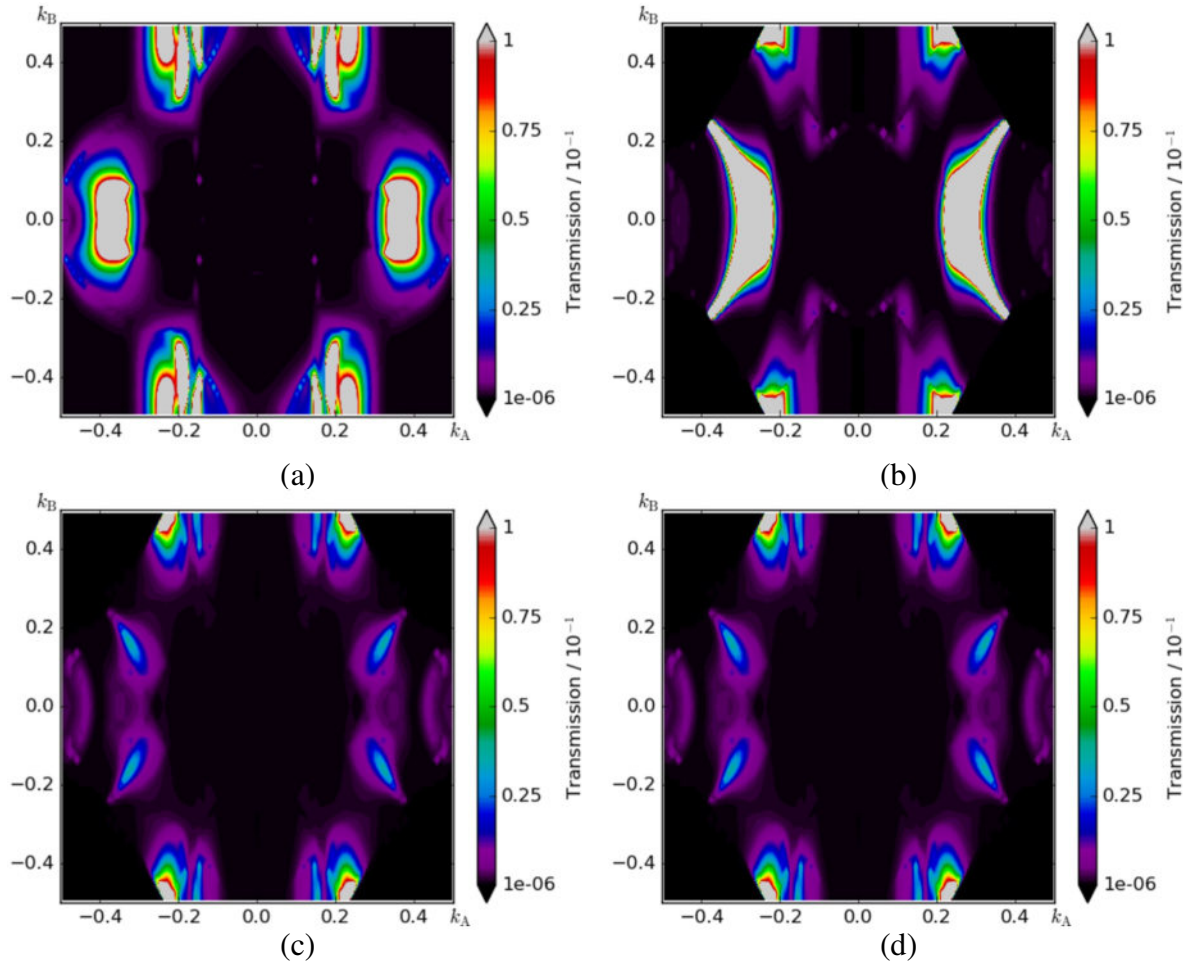


Figure 9 K -resolved transmission spectrum in spin-up (left panel) and spin-down channel (right panel) of $Fe(001)/Mo_xCr_{1-x}S_2(3\text{-layer})/Fe(001)$ junction in parallel (figure a, b) and anti-parallel (figure c, d) orientation of electrodes.

The spatial resolved local DOS (LDOS) along the transport z -direction in the PLDOS for the junction in Figure 10 shows that the conduction band for the Cr-doped MoS_2 middle layer in the spin-up channel has lowered after substitutional doping of Cr in MoS_2 . The three-layer $Mo_xCr_{1-x}S_2$ spacer is metallic, and the metal-induced states in MoS_2 due to the interface with Fe are seen from the PLDOS for both spin-up and spin-down channels.

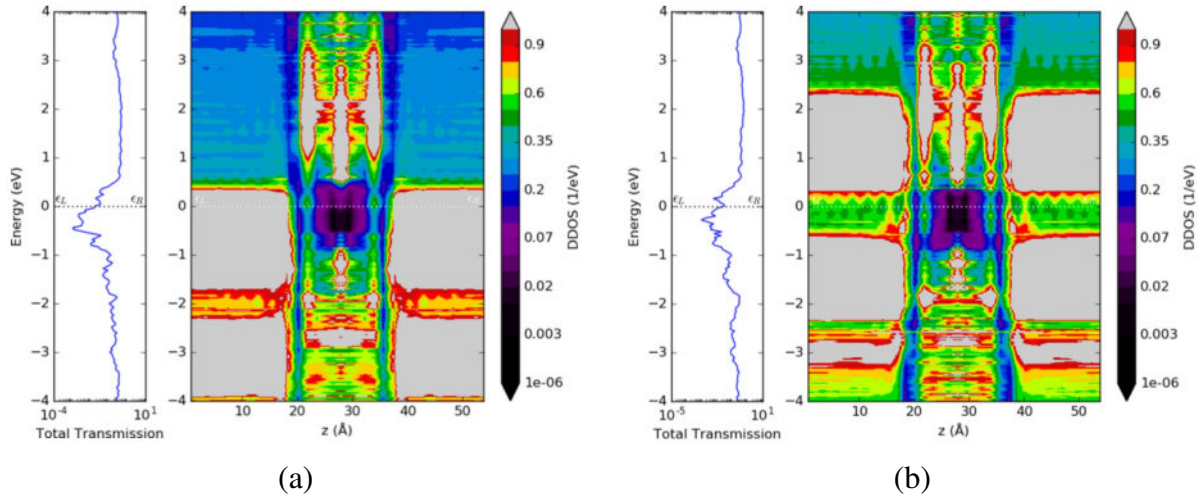


Figure 10 PLDOS for spin-up (a) and spin-down (b) channel in $Fe(001)/Mo_xCr_{1-x}S_2(3\text{-layer})/Fe(001)$ junction in parallel orientation of electrodes.

$Fe(001)/MoS_2(5\text{-layer})/Fe(001)$ junction

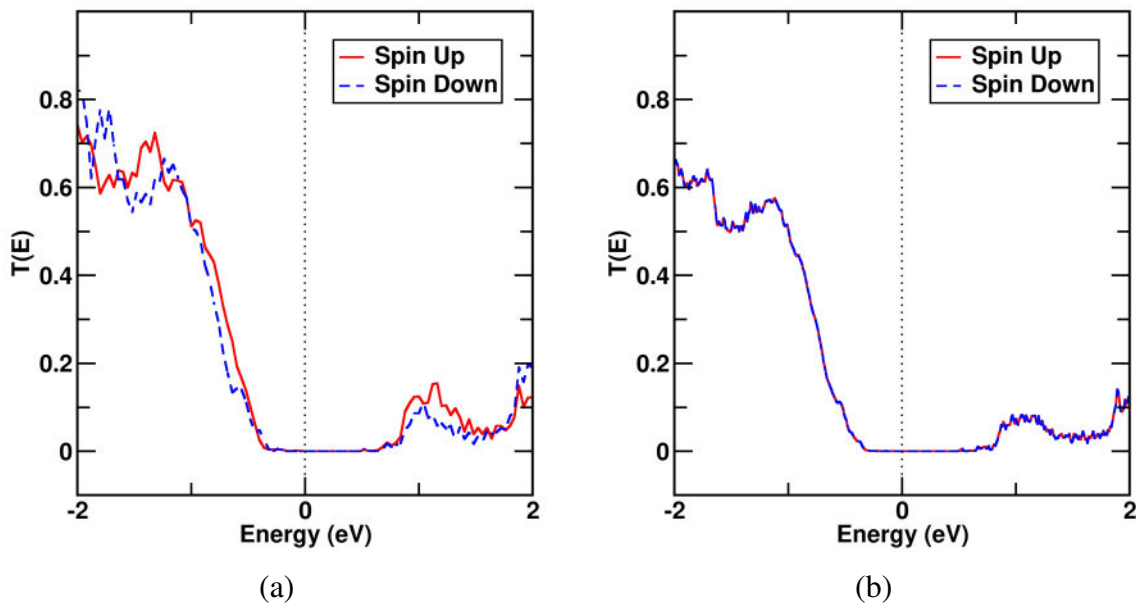


Figure 11 Transmission spectrum for $Fe(001)/MoS_2(5\text{-layer})/Fe(001)$ junction in parallel (a) and anti-parallel (b) orientation of electrodes.

Figure 11 Shows the transmission spectrum for the $Fe/MoS_2(5\text{-layer})/Fe$ junction. The transmission for the device in P orientation shows that the transmission with a spacer with a thickness of five layers of MoS_2 has significantly reduced at zero-bias for both the spin-up channel and spin-down channel, with values 0.0004 and 0.0002, respectively. For AP

orientation of electrodes, the transmission for spin-up and spin-down channels is the same and of the order of 10^{-4} .

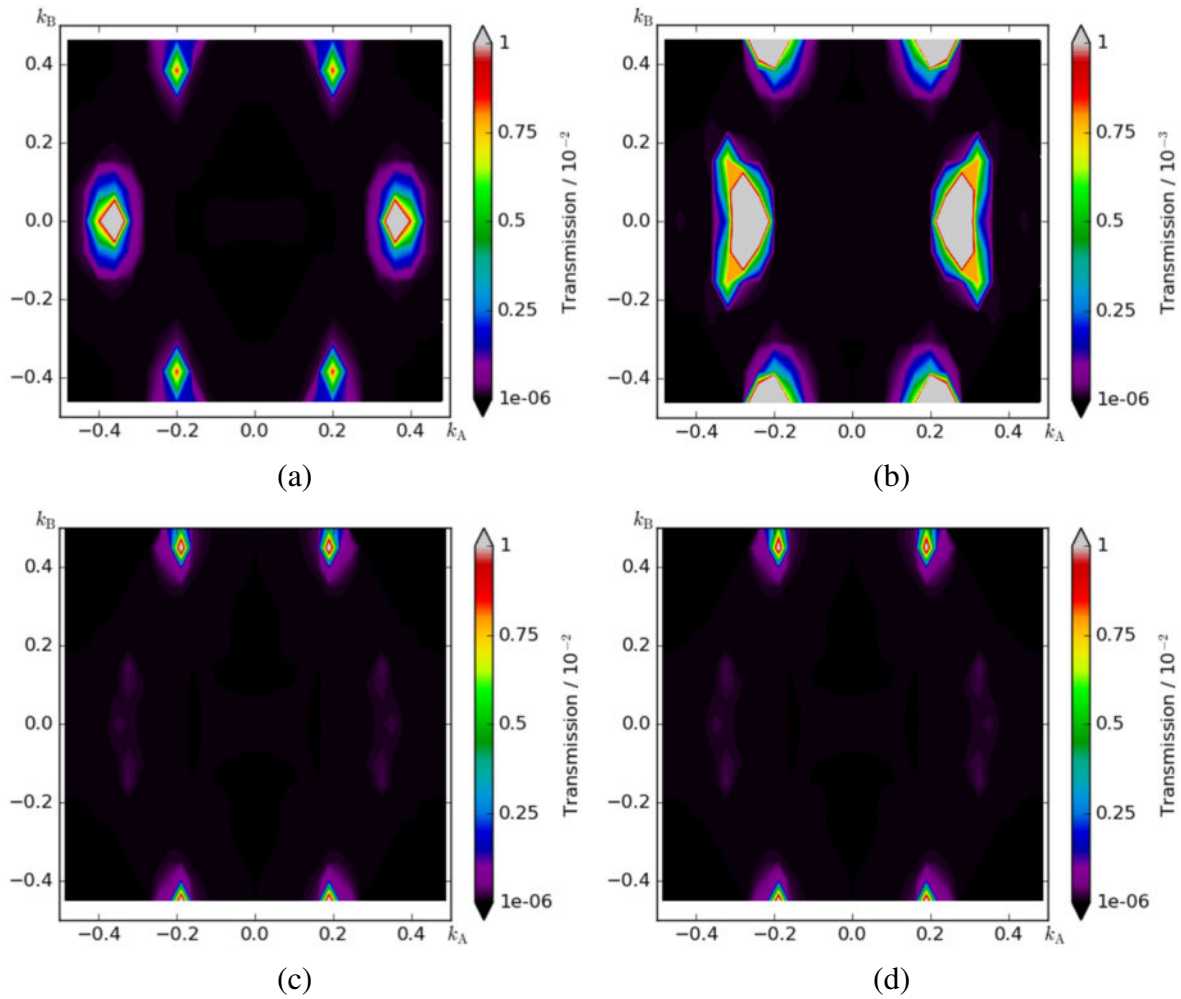


Figure 12 *K*-resolved transmission spectrum in spin-up (left panel) and spin-down (right panel) channel for Fe(001)/MoS₂(5-layer)/Fe(001) junction in parallel (figure a, b) and anti-parallel (figure c, d) orientation of electrodes.

The *K*-resolved transmission spectrum for the Fe/MoS₂(5-layer)/Fe junction for spin-up and spin-down channels in P and AP is shown in Figure 12. The 2D colour map representing the *K*-resolved transmission spectrum shows the transmission co-efficient contributing to the transmission from the entire 2D Brillouin zone. The transmission coefficient for both the spin-up and spin-down channels in P shows a maximum coefficient of order 10^{-2} that comes from six pockets away from the centre of the hexagonal 2D Brillouin zone. For the junction in AP orientation of the electrodes, transmission co-efficient for the

spin-up and spin-down are identical, a maximum contribution to the transmission comes from four points with a transmission coefficient of 10^{-3} .

The total DDOS for the five-layer device is shown in Figure 4.13(a), and the PDOS for the five-layer MoS_2 spacer in the device is shown in Figure 13(b). The PDOS for five-layer MoS_2 is metallic, and a small spin-polarisation in MoS_2 is observed from the PDOS. The PDOS for the three-layer MoS_2 Figure 14(a) shows that DOS for spin-up just crosses the Fermi level, whereas DOS has a narrow band gap in the spin-down channel. The PDOS for the single layer of MoS_2 layer in the middle layer of the junction in Figure 14(b) Shows a semiconducting band gap. Thus, the semiconducting nature of single-layer MoS_2 is retained by the middle layer, and the tunneling of electrons through the junction is due to the middle layer of MoS_2 . A small spin-polarisation is seen from the PDOS for three-layer and single-layer MoS_2 in the middle layer of the five-layer spacer.

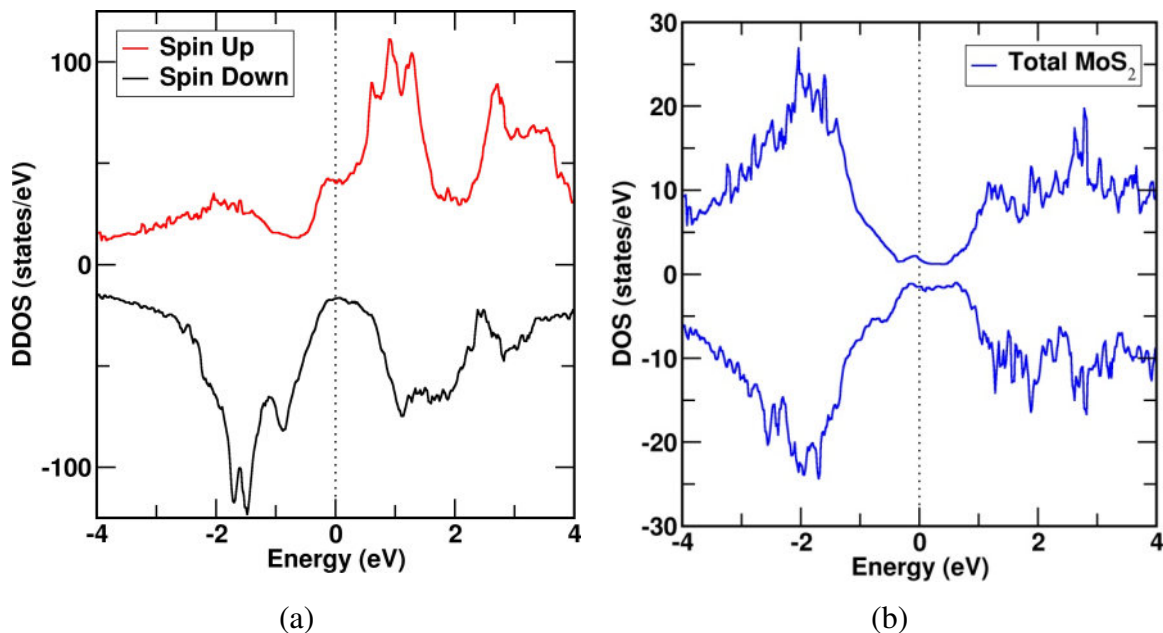


Figure 13 Total device DOS for the 5-layer device (a) and PDOS for 5-layers of MoS_2 (b) in the 5-layer device in the parallel orientation of electrodes.

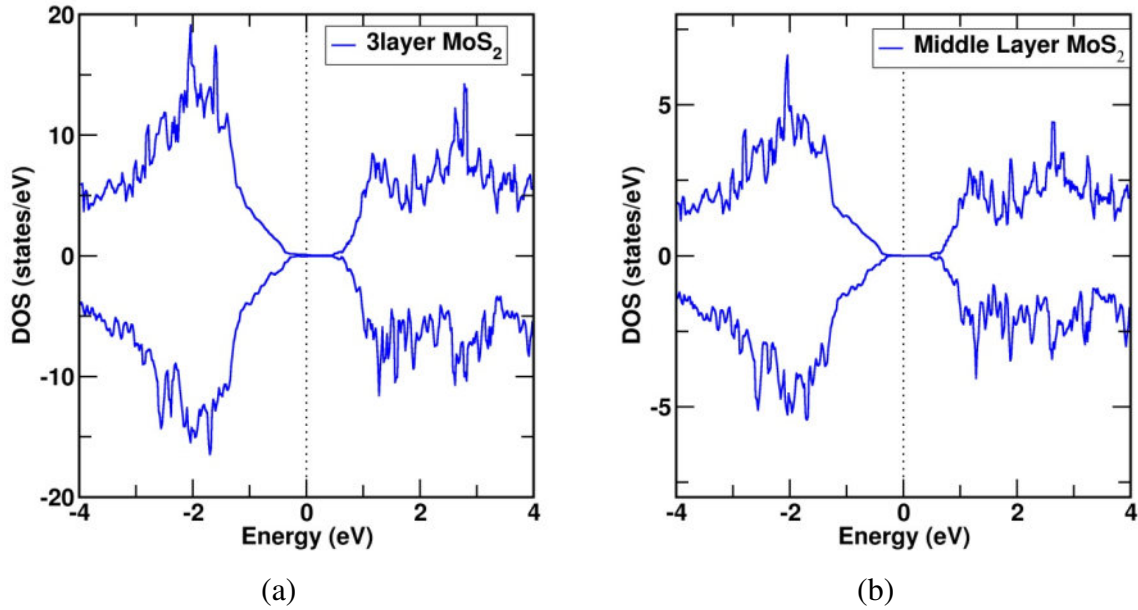


Figure 14 PDOS for three layers of MoS_2 (a) and middle layer MoS_2 (b) in $\text{Fe}(001)/\text{MoS}_2(5\text{-layer})/\text{Fe}(001)$ junction in the parallel orientation of electrodes.

The PLDOS for the $\text{Fe}/\text{MoS}_2(5\text{-layer})/\text{Fe}$ junction in P orientation is shown in Figure 15. From the PLDOS, the strong coupling between the ferromagnetic Fe layers and the first layer of MoS_2 at the Fe/MoS_2 interface is observed, and the coupling is strong enough for the next MoS_2 layer to induce metal-induced states on both sides of the interface. From the 2D colour map for the PLDOS, light green regions can be seen on both sides of the Fe/MoS_2 interface corresponding to the first layer of MoS_2 at the interface, showing the presence of states in the band gap region of MoS_2 . The metallicity of interface MoS_2 arises from the strong hybridisation of Fe d -orbitals with d -orbitals of Mo and p -orbitals of S. For the next layer of MoS_2 at the interface, only the spin-up channel crosses the Fermi-level, as seen in the PDOS for the three-layer MoS_2 in Figure 14(a). The middle layer of MoS_2 retains its semiconducting nature, as seen in both PLDOS in Figure 4.15 and PDOS for the middle layer in Figure 14(b). Thus, the effect of coupling is limited to the first two layers of MoS_2 at the Fe/MoS_2 interface.

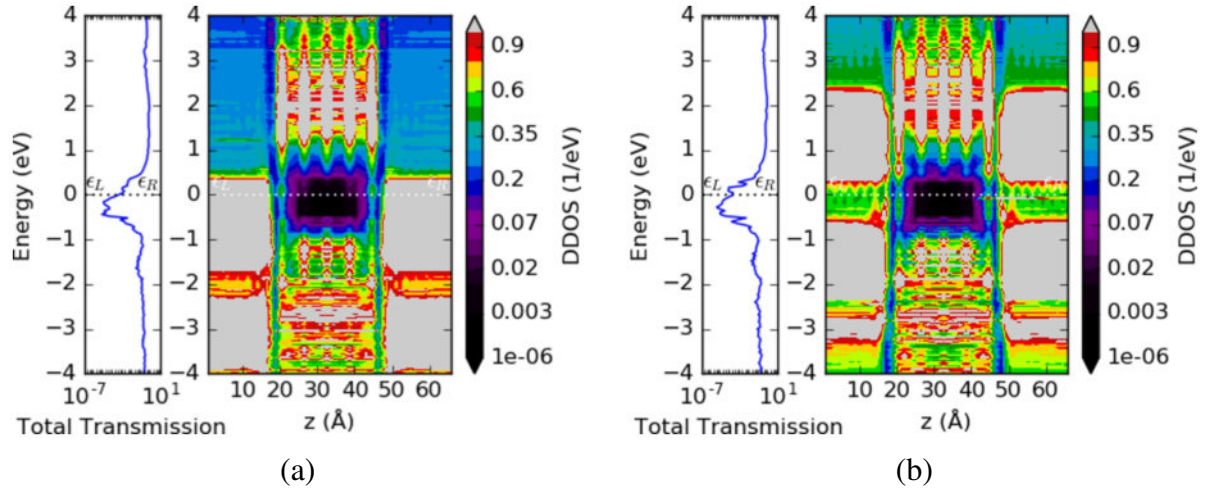


Figure 15 PLDOS for spin-up (a) and spin-down (b) channel in Fe(001)/MoS₂(5-layer)/Fe(001) junction in parallel orientation of electrodes.

The spin-dependent transmission for Fe/MoS₂(5-layer)/Fe device doped with magnetic impurity Cr in the middle layer of five-layer MoS₂ at zero-bias condition is shown in Figure 16. The P orientation has transmission of 1.5×10^{-4} in spin-up, and spin-down has the order of 10^{-5} at the Fermi-level under zero-bias, as shown in Figure 16(a). For the AP orientation of electrodes, the junction has transmission of 3.5×10^{-5} for both spin-up and spin-down channels at the zero-bias condition, as shown in Figure 16(b).

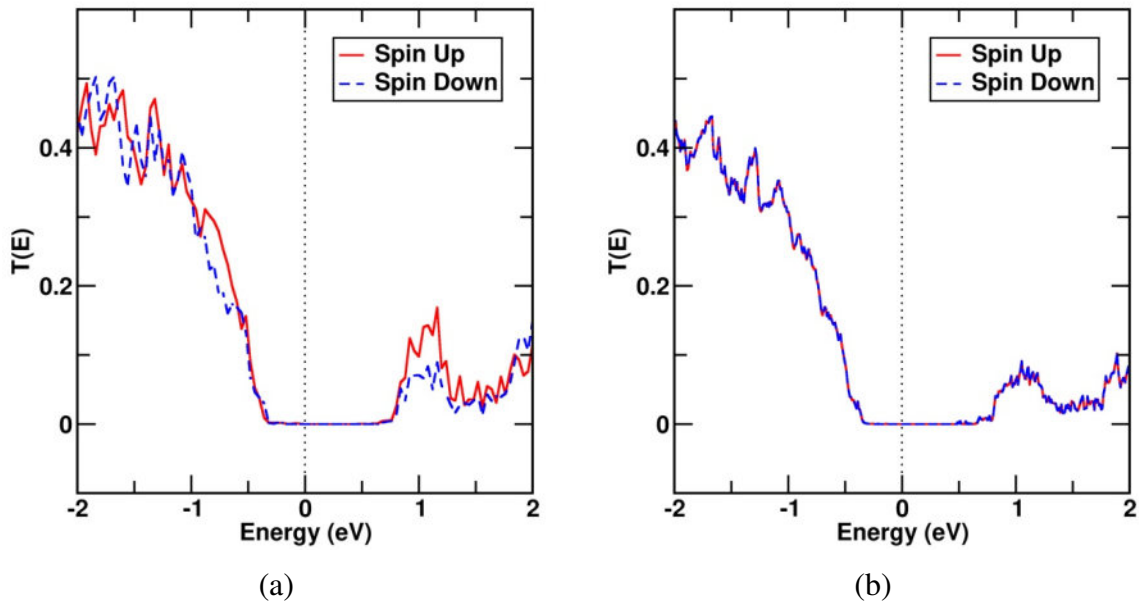


Figure 16 Transmission spectrum for Fe(001)/Mo_xCr_{1-x}S₂(5-layer)/Fe(001) in parallel (a) and anti-parallel (b) orientation of electrodes.

The K-resolved transmission spectrum for the junction in P orientation is shown in Figure 17. From the 2D colour map of the K-resolved transmission spectrum, six pockets in the 2D Brillouin zone contributing a maximum transmission coefficient of the order of 2×10^{-3} for the spin-up channel and 1×10^{-3} for the spin-down channel are observed.

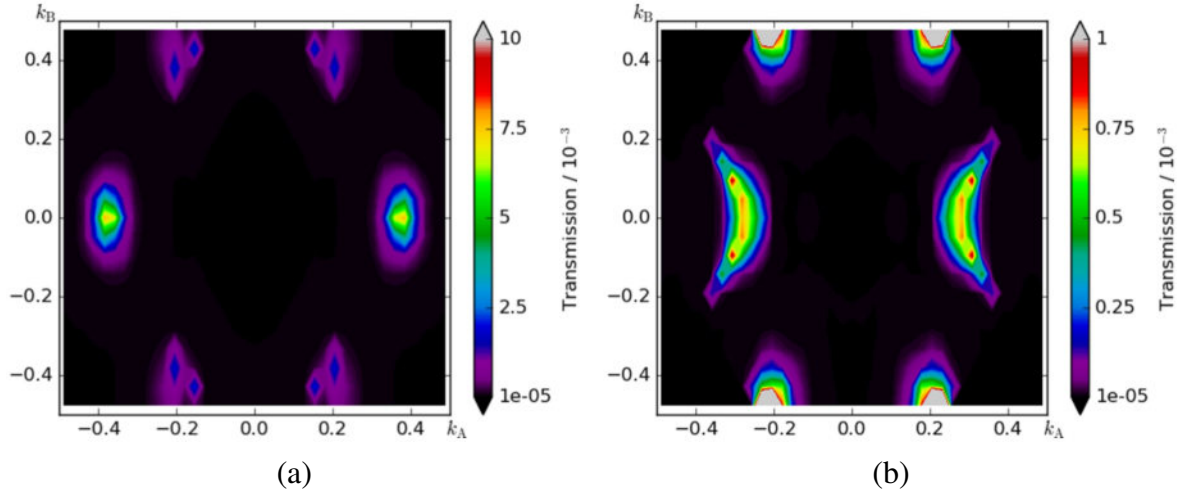


Figure 17 K-resolved transmission spectrum in spin-up (a) and spin-down (b) channel for $Fe(001)/Mo_xCr_{1-x}S_2(5\text{-layer})/Fe(001)$ junction in parallel orientation of electrodes.

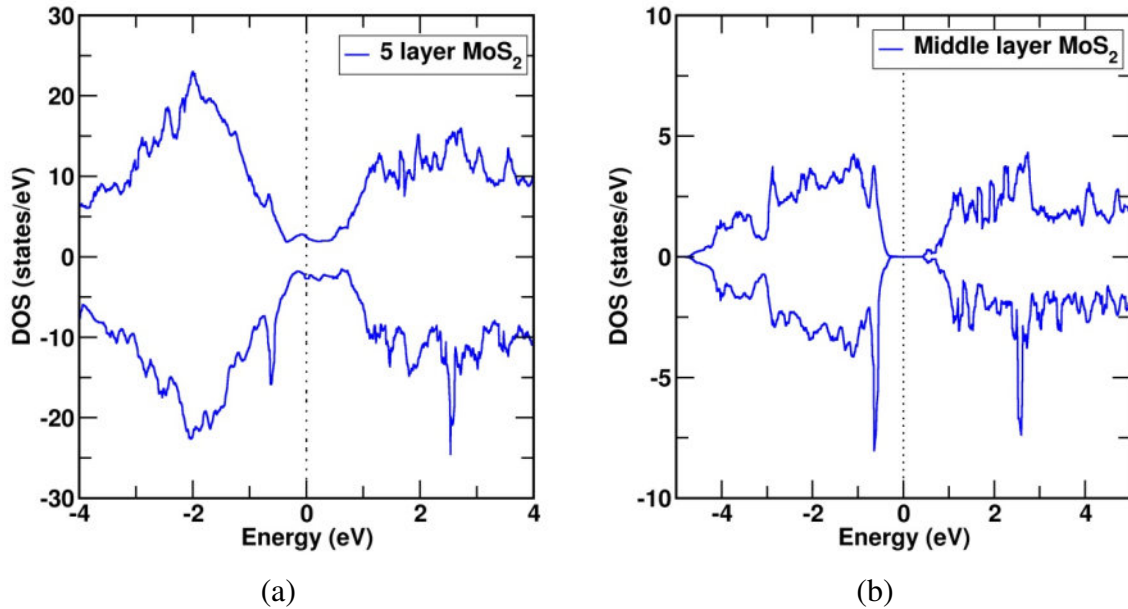


Figure 18 PDOS of Cr-doped 5-layer MoS_2 (a) and Cr-doped MoS_2 middle layer (b) in parallel orientation of electrodes.

PDOS for the Cr-doped five-layer MoS_2 and middle layer of MoS_2 in the junction is shown in Figure 18. The five-layer Cr-doped MoS_2 is metallic, and a small spin-polarisation

of the DOS is seen. For the middle layer of MoS₂ in which the magnetic impurity Cr is substituted at the Mo Site, the PDOS in Figure 18(b) shows that the single layer of thick MoS₂ is semiconducting and an increase in spin-polarisation of the DOS is observed after the Cr doping.

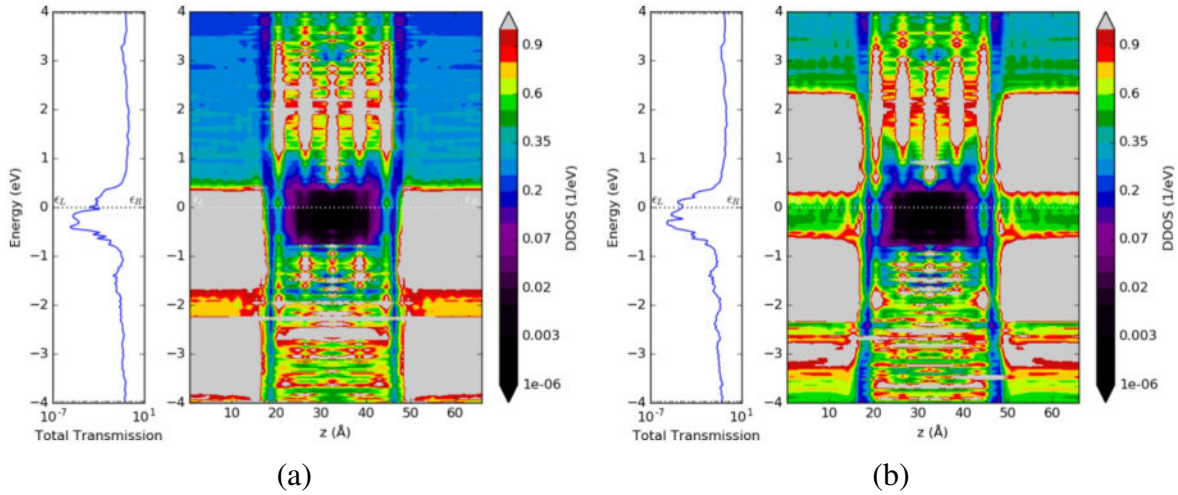


Figure 19 PLDOS for spin-up (a) and spin-down channel (b) in Fe(001)/Mo_xCr_{1-x}S₂(5-layer)/Fe(001) junction in parallel orientation of electrodes.

The PLDOS of the Fe/Mo_xCr_{1-x}S₂(5-layer)/Fe junction in P orientation is shown in Figure 19. The 2D colour map for the PLDOS shows a similar observation that is observed for the 5-layer device where the first layer of MoS₂ on both sides of the junction at the Fe/MoS₂ interface is metallic, having a higher number of metal-induced states in the bandgap region of MoS₂. For the second layer of MoS₂ on both sides of the junction at the Fe/MoS₂ interface, the spin-up channel shows a small number of states present at the fermi level, and the spin-down channel shows the absence of states. After doping Cr in the middle layer of five-layer MoS₂, the PLDOS shows that the conduction band for the middle layer has come down, as seen from the bright, lighter regions for the LDOS of the middle layer in Figure 19. Thus, after Cr doping, the bandgap for the Cr-doped MoS₂ has reduced due to the presence of Cr-defect levels in the bandgap region as observed in previous studies [77,78].

Fe(001)/MoS₂(7-layer)/Fe(001) junction

The transmission spectrum for the junction with seven-layer MoS₂ as a spacer at zero-bias is shown in Figure 20. The transmission spectrum for the junction across the spin-up and spin-down channel is 1.6×10^{-5} and 1.75×10^{-6} , respectively as shown in Figure 20(a). For the AP orientation of the electrodes, the transmission spectrum is the same for both channels and has a transmission of the order of 10^{-6} for both spin-up and spin-down channels as shown in Figure 20(b).

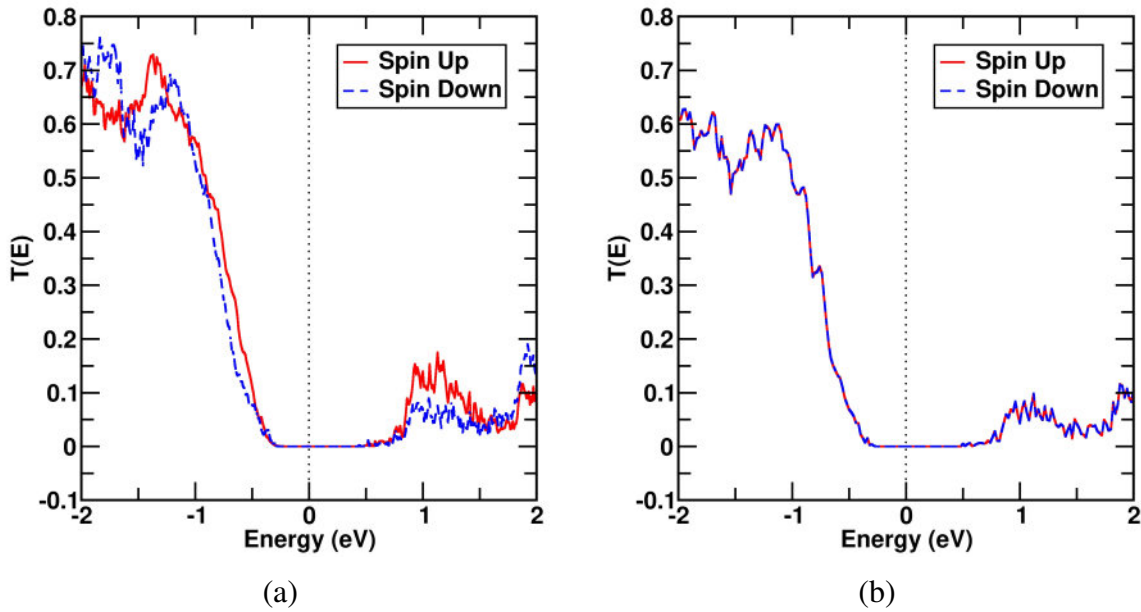


Figure 20 Transmission spectrum for *Fe(001)/MoS₂(7-layer)/Fe(001)* junction in parallel (a) and anti-parallel (b) orientation of electrodes.

The K-resolved transmission spectrum for the spin-up and spin-down channels in the P orientation of the electrode is shown in Figure 21. The 2D colour map for the K-resolved transmission spectrum shows transmission co-efficient contributing to the total transmission from the 2D Brillouin zone of the device. The transmission coefficient for spin-up and spin-down channels having a maximum contribution to the transmission of the order 10^{-4} comes from six pockets away from the Brillouin zone centre. The transmission coefficient for the spin-down channel is higher than the spin-up channel. The *Fe/MoS₂(7-layer)/Fe* junction,

with seven MoS₂ layers as a spacer, is thick enough to reduce transmission through the junction to the order of 10⁻⁶, and the transmission through the junction occurs only due to tunneling of electrons.

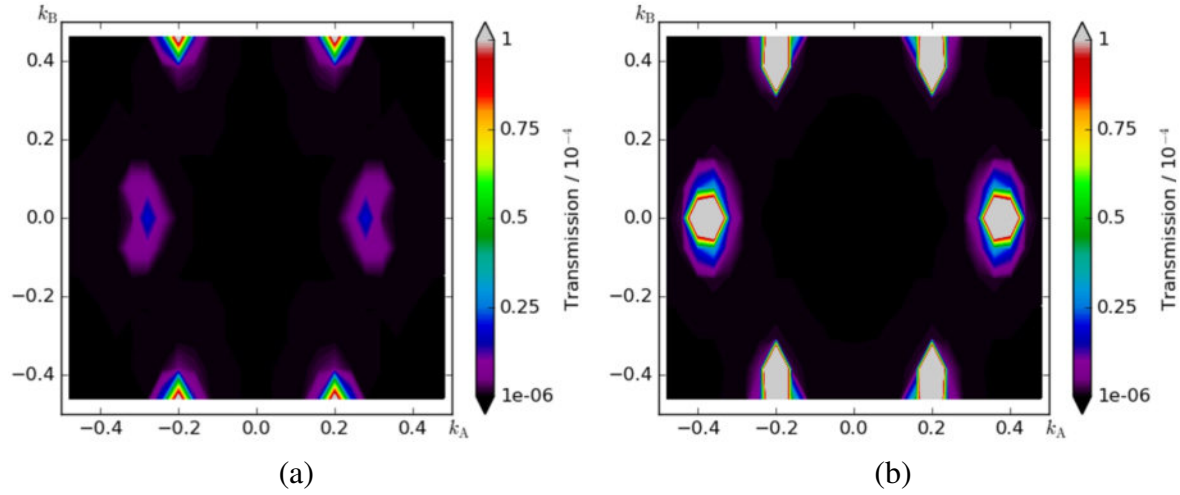


Figure 21 *K*-resolved transmission spectrum in spin-up (a) and spin-down (b) channel of Fe(001)/MoS₂(7-layer)/Fe(001) junction in the parallel orientation of electrodes.

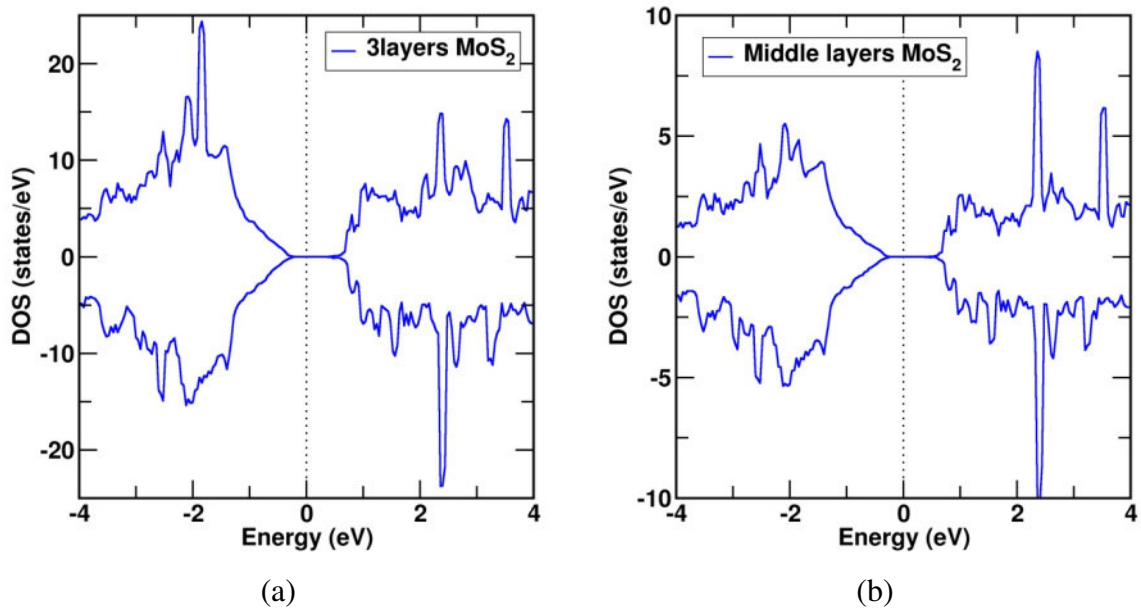


Figure 22 PDOS for three layers of MoS₂ and single layer MoS₂ in 7-layer MoS₂.

The PDOS for three-layer and one-layer thick MoS₂ in the middle of the seven-layer thick MoS₂ spacer is shown in Figure 22. The PDOS in Figure 22 shows that the one layer and the three layers of the seven-layer thick spacer maintain the semiconducting nature of the

bandgap for MoS₂. Spin-polarisation of the DOS for the three-layer and one-layer thick MoS₂ is observed, and the spin-polarised PDOS for the one-layer and three layers are similar to the DOS for bulk semiconducting MoS₂. The spin-polarisation of MoS₂ is due to the interface with ferromagnetic Fe. Thus, the spin-polarisation and semiconducting nature of PDOS shows that electrons can only tunnel through the seven-layer thick MoS₂ as a spacer in the Fe/MoS₂/Fe junction.

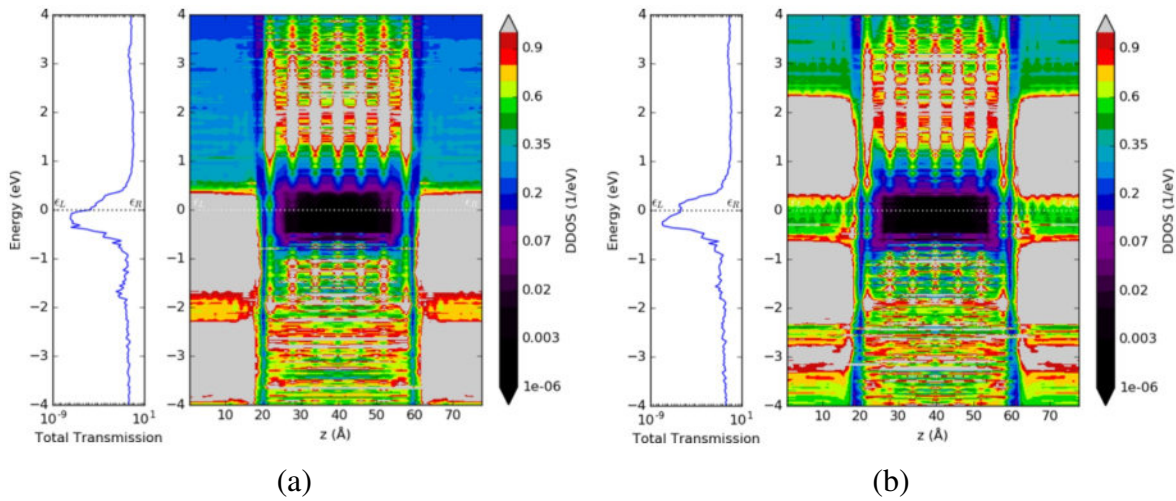


Figure 23 PLDOS for spin-up (a) and spin-down (b) channel in Fe(001)/MoS₂(7-layer)/Fe(001) junction in parallel orientation of electrodes.

The PLDOS for the device shown in Figure 23 This shows that the interface effect is only limited to the first two layers of MoS₂ close to the interface, where the strong coupling with the Fe layers introduces metal-induced states in the first two MoS₂ layers near the interface. The subsequent three layers of MoS₂ next to the interface layer in the middle of the 7-layer MoS₂ retain the semiconducting nature of the band gap.

The transmission spectrum for seven layers of thick MoS₂ doped with Cr in the middle layer of MoS₂, in P and AP orientation of electrodes under zero-bias condition, is shown in Figure 24. Transmission spectrum for both P and AP orientation of electrodes at the fermi level is of the order of 10⁻⁶ as shown in Figure 24(a) and for AP, the transmission spectrum is identical for both spin-up and spin-down channels, as shown in Figure 24(b).

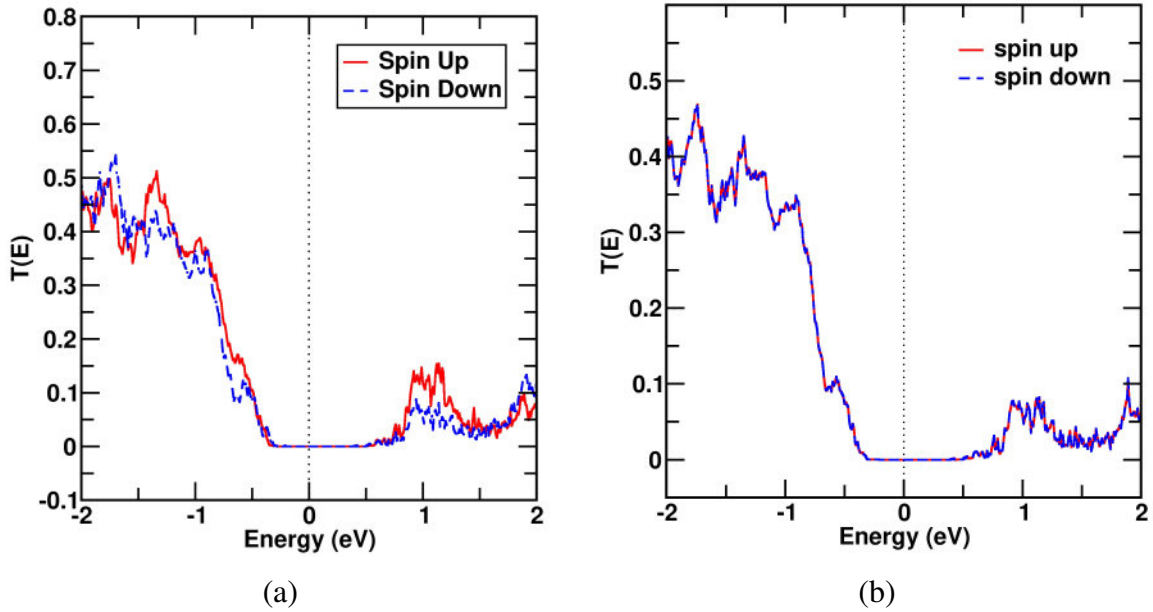


Figure 24 Transmission spectrum for $Fe(001)/Mo_xCr_{1-x}S_2(7\text{-layer})/Fe(001)$ junction in the parallel and anti-parallel orientation of electrodes.

Corresponding K-resolved transmission spectrum to the Figure 24 is shown in Figure 25 and Figure 26(b). The 2D colour map for the spin-up channel in P shows six points from the 2D Brillouin zone contribute to the total transmission with a maximum contribution of the order of 10^{-4} for the spin-down two points from the 2D Brillouin zone contributes a maximum transmission of the order of 10^{-4} . For the AP orientation of electrodes, the spin-up and spin-down channels are identical, and the contribution from 2D the Brillouin zone is of the order of 10^{-5} , as seen in Figure 26(b).

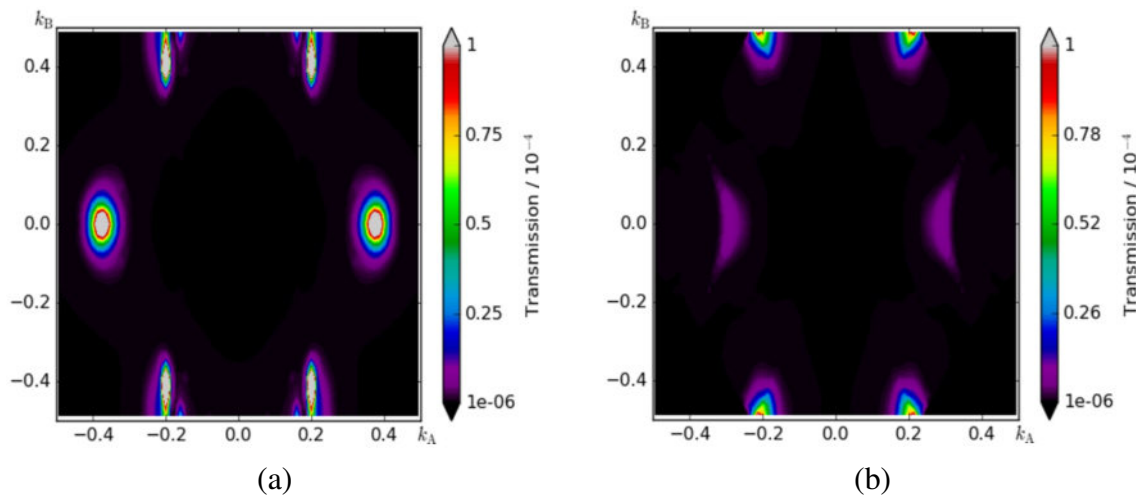


Figure 25 K -resolved transmission spectrum for spin-up (a) and spin-down channel (b) of $Fe(001)/Mo_xCr_{1-x}S_2(7\text{-layer})/Fe(001)$ junction in parallel orientation of electrode.

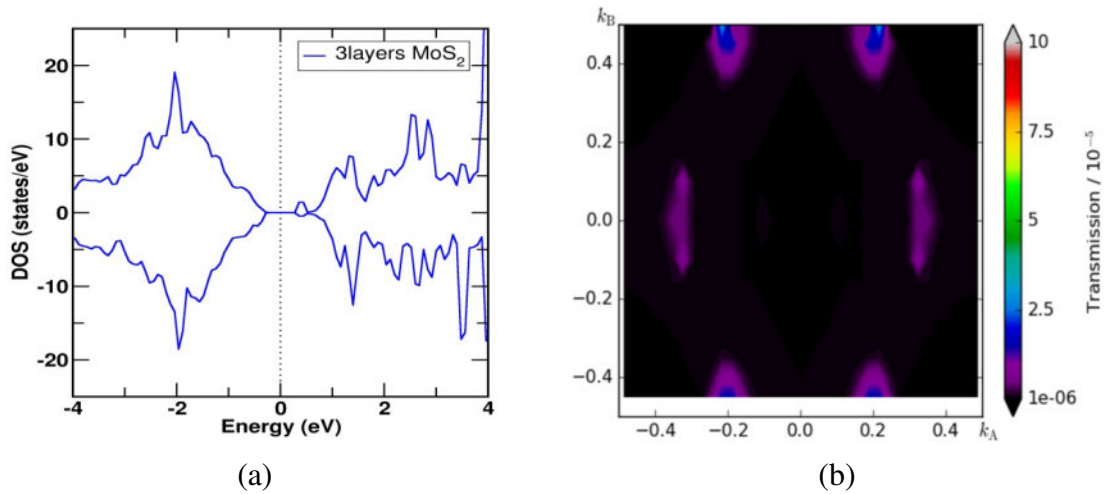


Figure 26 PDOS for three layers of MoS_2 layers in a 7-layer Cr-doped device and K -resolved transmission for $Fe(001)/Mo_xCr_{1-x}S_2(7\text{-layer})/Fe(001)$ junction in anti-parallel orientation.

The PDOS for the Cr-doped middle layer of MoS_2 in the seven-layer MoS_2 is shown in Figure 26(a). The PDOS shows the semiconducting nature of the Cr-doped MoS_2 single layer. Small spin-polarisation of DOS and Cr defect level near the conduction band is observed. The presence of states in the band gap region of the Cr-doped middle layer MoS_2 can be seen from the PLDOS of the device, as shown in Figure 27. The availability of states due to the presence of Cr defect level is observed from the extended bright red regions for the LDOS of the Cr-doped middle layer MoS_2 .

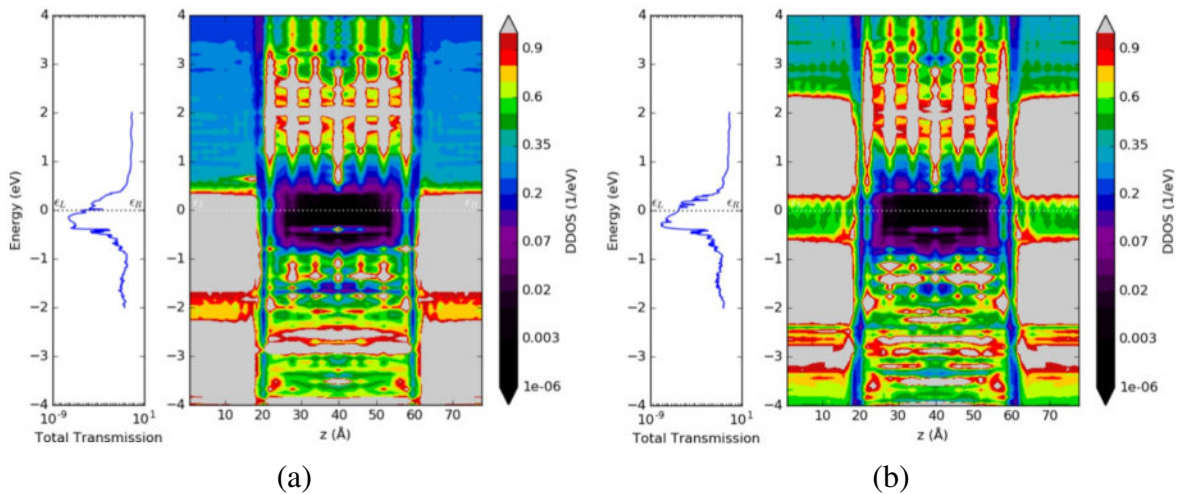


Figure 27 PLDOS for spin-up (a) and spin-down (b) channel in $Fe(001)/Mo_xCr_{1-x}S_2(7\text{-layer})/Fe(001)$ junction in parallel orientation of electrodes.

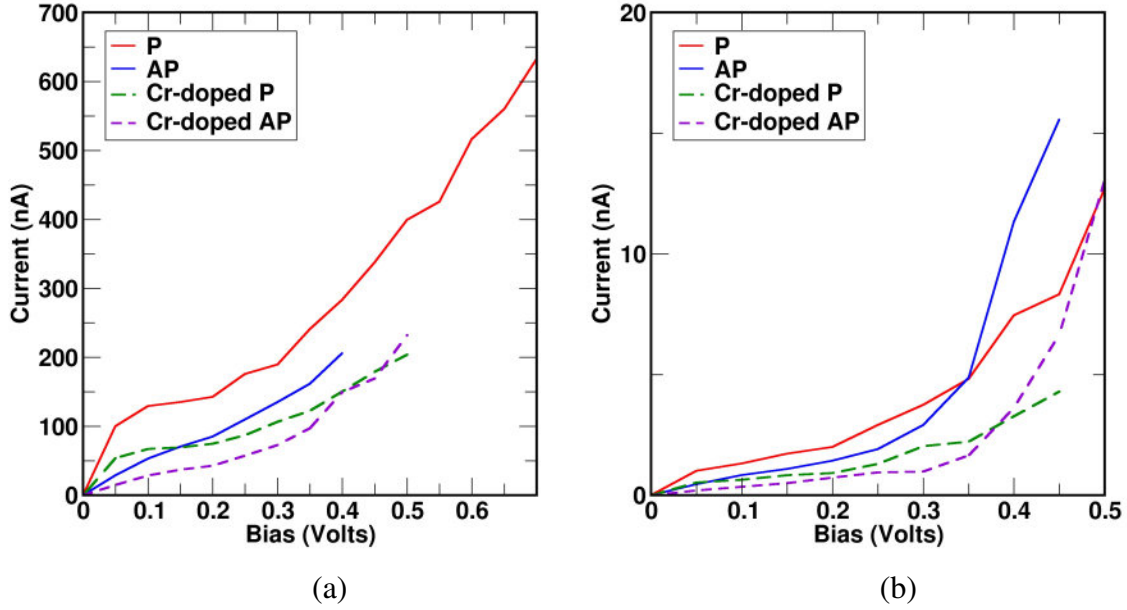


Figure 28 I-V plot for undoped and doped 3-layer device (a), and for 5-layer undoped and doped device (b).

The I-V plot for the 3-layer device with Cr-doped MoS_2 and undoped MoS_2 three-layer as spacer is shown in Figure 28 (a). The I-V plot for the 3-layer device shows linear behaviour due to the metallic nature of the first MoS_2 layer and the half-metallic nature of the next layer at the interface. The device is stable up to a bias of 0.5V, and the spin current for the parallel configuration is higher than that of the anti-parallel configuration. For 5-layer MoS_2 as a spacer, the spin-current has further reduced and is of the order of 10 nano-Ampere as the interface of effect is only limited to the first two layers of MoS_2 . The tunnelling behaviour of electrons in the junction is observed. After a bias of 0.35V, the spin current for the anti-parallel configuration is higher than that of the parallel configuration. This is also seen in the K-resolved transmission spectrum in Figure 17 (b) for the device where the transmission coefficient for the spin-down channel is higher than the spin-up channel. The 5-layer device is stable up to a bias of 0.5V. The bias range for the device is understandable because the band of MoS_2 is of the order of 0.7V with LDA approximation, where we see that

with Cr doping in the MoS₂ layer, the presence of Cr-defect levels below the conduction band. I-V characteristics for the junction with 7-layer MoS₂ as the spacer are shown in Figure 29 (a). The device is stable up to a bias of 0.7V and 0.5V for undoped MoS₂ and for Cr-doped MoS₂, respectively. The tunnelling nature of the junction is observed as the three-middle layers of 7-layer MoS₂ keep the semiconducting nature of the bulk MoS₂.

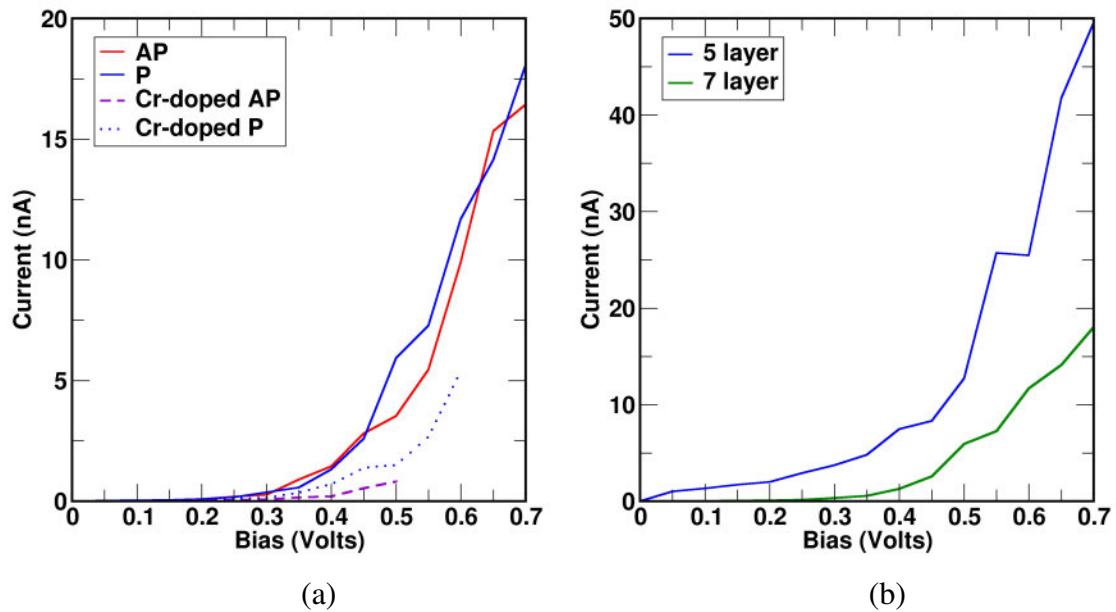


Figure 29 I-V plot for undoped and doped devices for 7-layer device (a) and five and 7-layer devices in parallel configuration (b).

Spin transport in Fe(111)/MoS₂/Fe(111) Junction

Fe(111)/MoS₂(1-layer)/Fe(111) junction

Figure 30(a) shows the DOS for the Fe(111)/MoS₂(1 layer)/Fe(111), and Figure 30(b) shows PDOS for single-layer MoS₂ in the junction. PDOS for the MoS₂ shows the presence states at the Fermi-level for the single layer MoS₂ as a spacer, and spin-polarisation for spin-up and spin-down channels is observed. The strong hybridisation of Fe *d*-orbitals with *p*-orbitals of S and *d*-orbitals of Mo at the interface leads to the metallic nature of the interface MoS₂ layer.

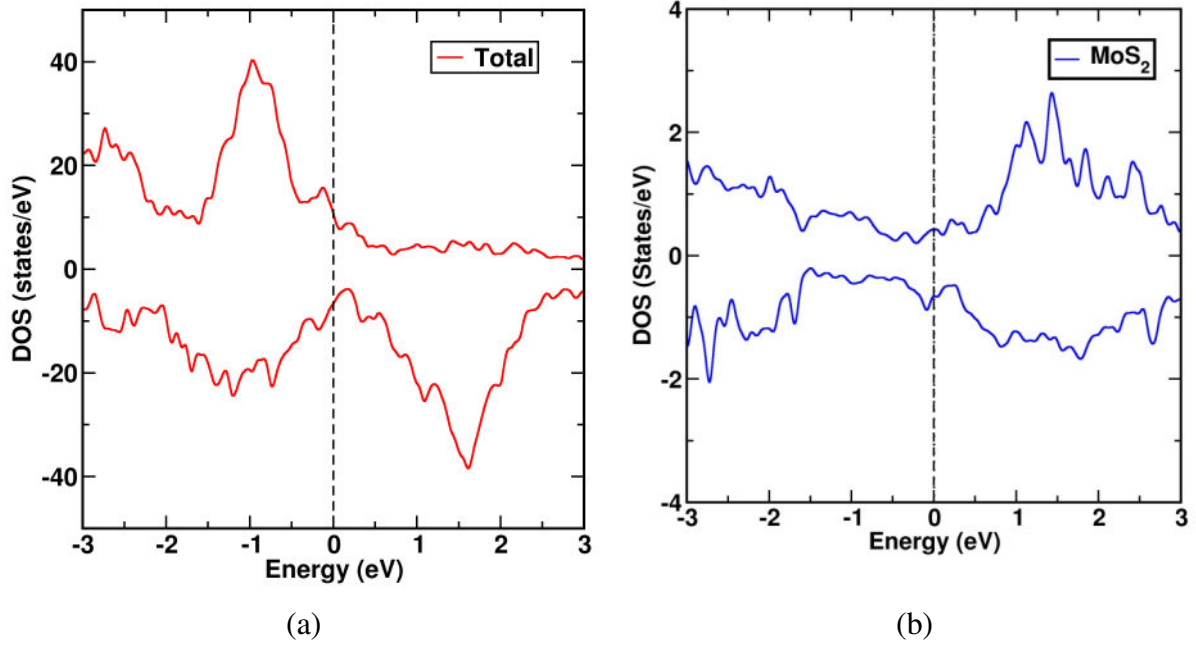


Figure 30 Total device DOS (a) and PDOS of single layer MoS_2 (b) in $\text{Fe}(111)/\text{MoS}_2(1\text{-layer})/\text{Fe}(111)$ junction.

The PLDOS for the $\text{Fe}(111)/\text{MoS}_2(1\text{-layer})/\text{Fe}(111)$ junction is shown in Figure 31. The 2D colour map for the PLDOS shows the effect of interface Fe layers on the LDOS of MoS_2 for both spin-up and spin-down channels. With the presence of metal-induced states in both channels of the single-layer MoS_2 spacer, the number of states available at the fermi level of MoS_2 is higher for the spin-down channel than for the spin-up channel.

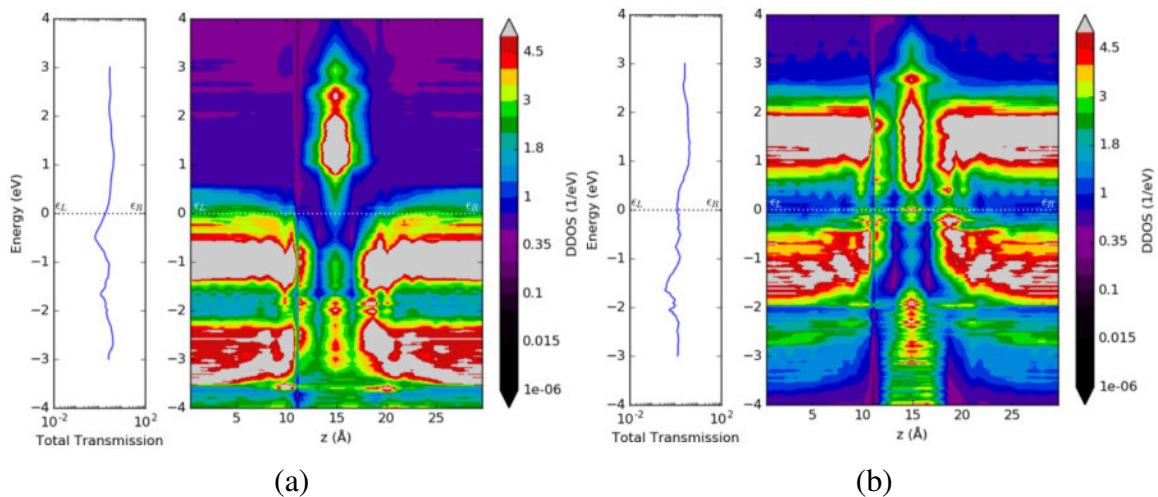


Figure 31 PLDOS of $\text{Fe}(111)/\text{MoS}_2(1\text{-layer})/\text{Fe}(111)$ junction in the parallel orientation of electrodes for spin-up (a) and spin-down (b) channel.

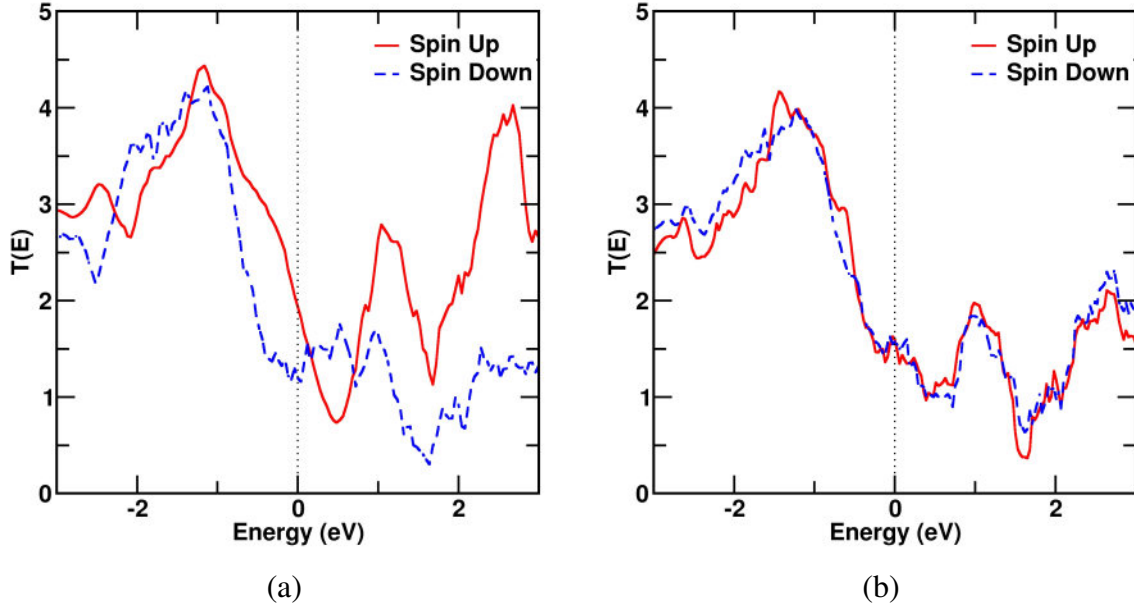


Figure 32 Transmission spectrum for Fe(111)/MoS₂(1-layer)/Fe(111) junction in parallel (a) and anti-parallel (b) orientation of electrodes.

The transmission spectrum for P and AP of the electrodes in the Fe(111)/MoS₂(1-layer)/Fe(111) junction under zero-bias condition is shown in Figure 32. For the parallel orientation of the electrode, the transmission for spin-up and spin-down channels at the fermi level is 1.89 and 1.26, respectively. The metallic nature of the junction leads to higher transmission at the zero-bias. Under the AP orientation of the electrodes, the transmission across the spin-up and spin-down channels is identical; the transmission at the fermi level for the channel is 1.63.

The K-resolved transmission spectrum for the Fe(111)/MoS₂(1-layer)/Fe(111) junction in P and AP is shown in Figure 33 and Figure 34 respectively. The 2D colour map for the K-resolved transmission spectrum of spin channels shows transmission co-efficient contributing to the total transmission at the fermi level from the 2D Brillouin zone. In the parallel orientation of the electrodes, the spin-up channel gets a contribution from the entire 2D Brillouin zone having a transmission coefficient of 1 from all the parts and the major contribution comes from the six corners close to the centre of the 2D hexagonal Brillouin

zone. For the spin-down channel, the transmission coefficient has a maximum value of 3 from the six hexagonal arms of the hexagonal 2D Brillouin zone near the Brillouin zone centre. The major contribution comes from the region close to the Brillouin zone centre only. For the anti-parallel orientation of electrodes, the K-resolved transmission is a combination of both channels of the P case.

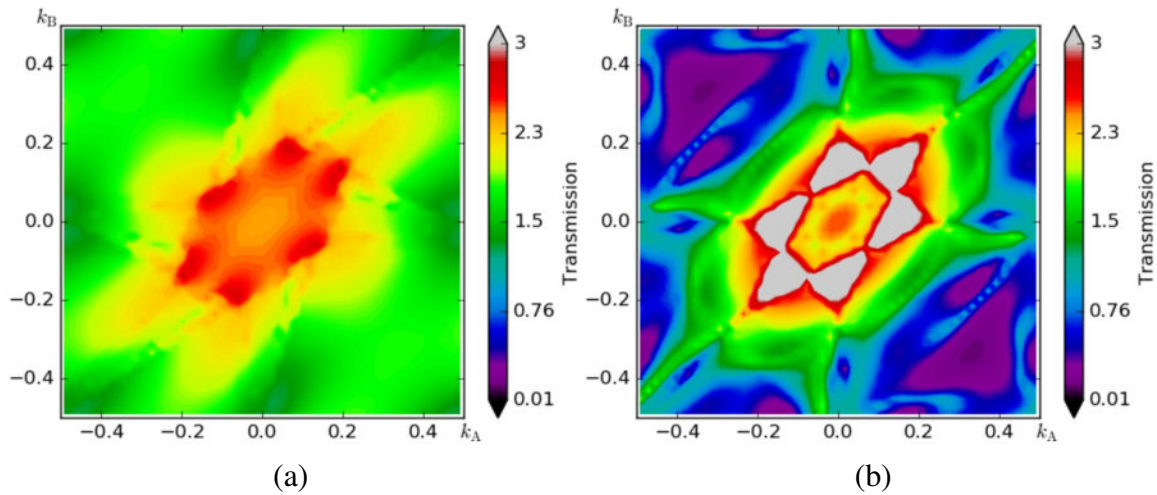


Figure 33 *K*-resolved transmission spectrum for spin-up (a) and spin-down channel (b) $Fe(111)/MoS_2(1\text{-layer})/Fe(111)$ junction in the parallel orientation of electrodes.

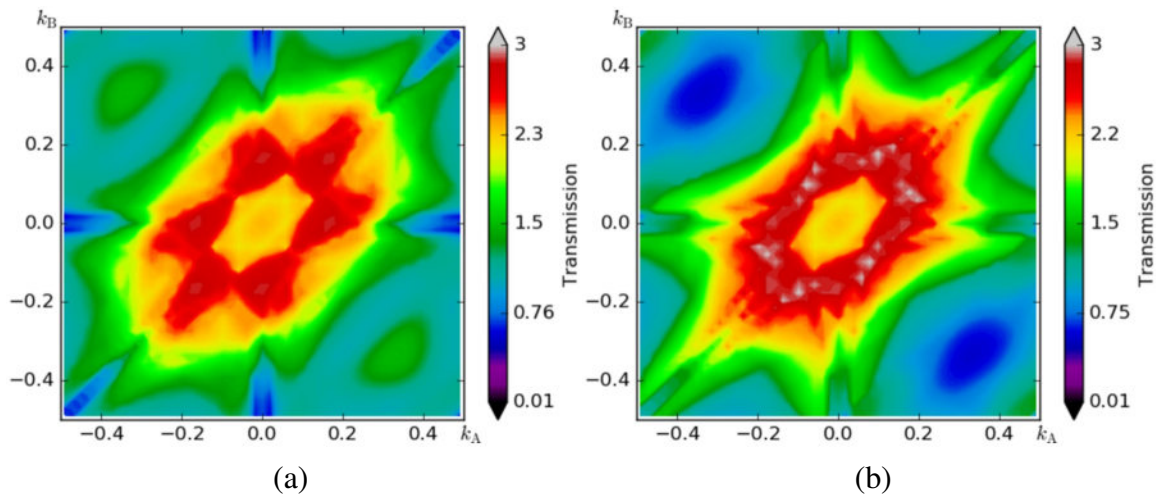


Figure 34 *K*-resolved transmission spectrum for spin-up (a) and spin-down (b) channel in $Fe(111)/MoS_2(1\text{-layer})/Fe(111)$ junction in the anti-parallel orientation of electrodes.

Fe(111)/MoS₂(3-layer)/Fe(111) junction

The spin-dependent transmission for the Fe(111)/MoS₂(3-layer)/Fe(111) junction in P and AP orientation of the electrodes under zero-bias conditions is shown in Figure 35. For the P orientation of electrodes under zero-bias, the transmission at the fermi level is 1.2×10^{-3} and 4×10^{-3} for spin-up and spin-down channels, respectively. For the AP orientation of electrodes, the transmission for both spin-up and spin-down channels is 2.0×10^{-3} and 2.6×10^{-3} , respectively.

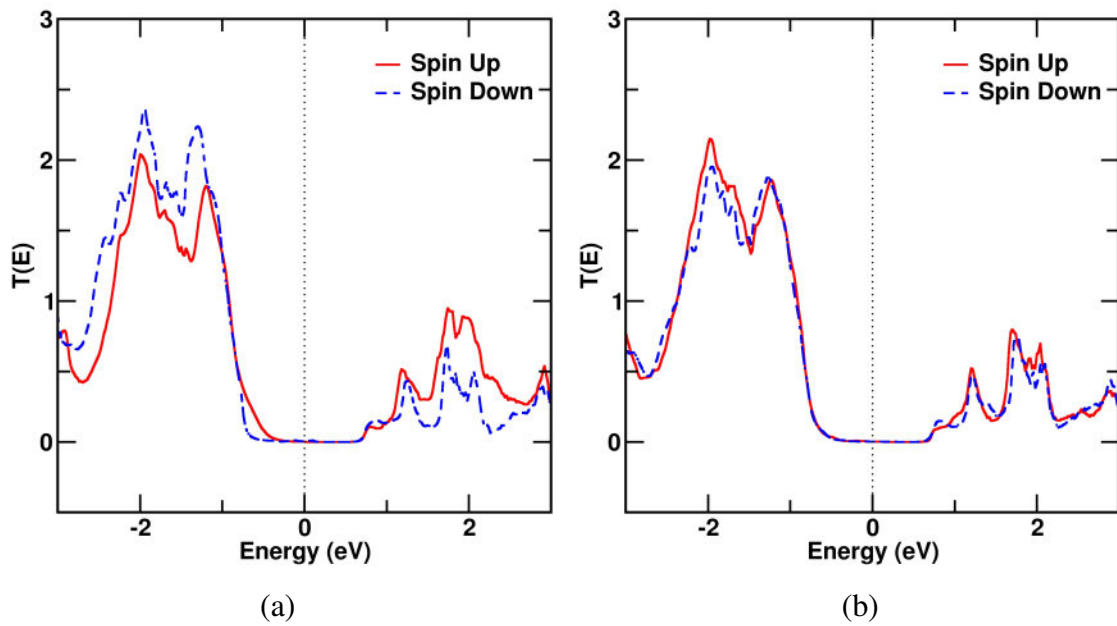


Figure 35 Transmission spectrum for Fe(111)/MoS₂(3-layer)/Fe(111) junction in parallel (a) and anti-parallel (b) orientation of electrodes.

The PDOS for three layers of MoS₂ as a spacer in the heterostructure is shown in Figure 36(a), and the PDOS for the middle layer of MoS₂ is shown in Figure 36(b). For the three-layer MoS₂, the interface also remains metallic, whereas the MoS₂ layer near the interface shows metallic behaviour. The PDOS for the middle layer of the three-layer MoS₂ shows that the DOS for spin-up and spin-down electrons crosses the Fermi level. Spin-polarisation for the middle layer MoS₂ is low, as seen from the spin-polarised PDOS for the middle layer MoS₂.

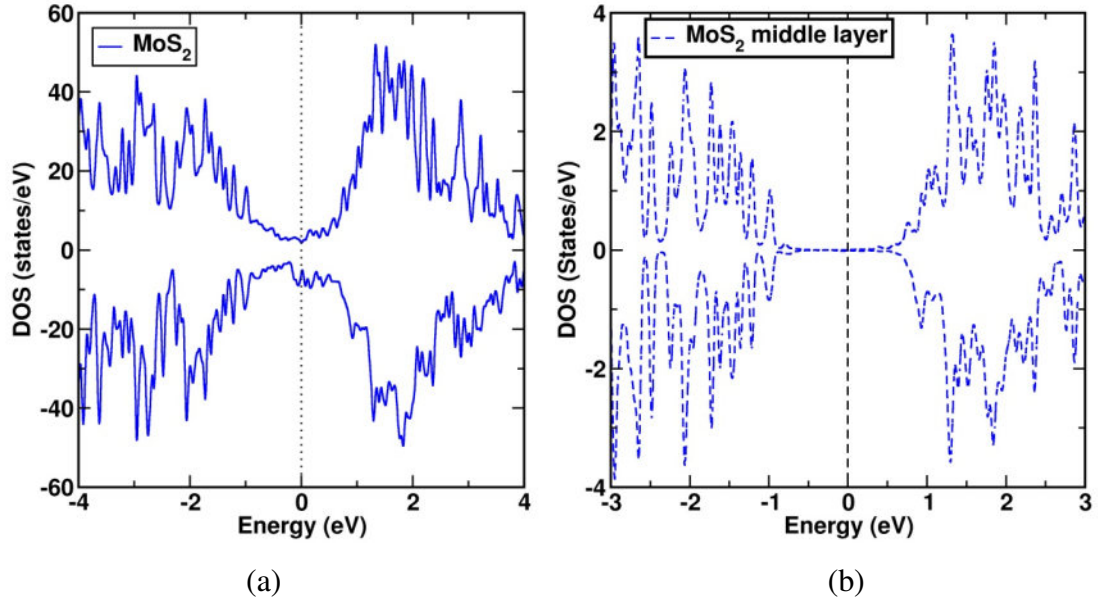


Figure 36 PDOS for three layers of MoS_2 and middle layer MoS_2 in the three layers in $\text{Fe}(111)/\text{MoS}_2(3\text{-layer})/\text{Fe}(111)$ junction.

The PLDOS for the $\text{Fe}(111)/\text{MoS}_2(3\text{-layer})/\text{Fe}(111)$ junction in P and AP is shown in Figure 37 and Figure 38, respectively. From the PLDOS of the junction, metal-induced states in the first layer of MoS_2 on both sides of the interface and the LDOS for middle layer MoS_2 shows DOS for spin-up and spin-down crossing the Fermi level.

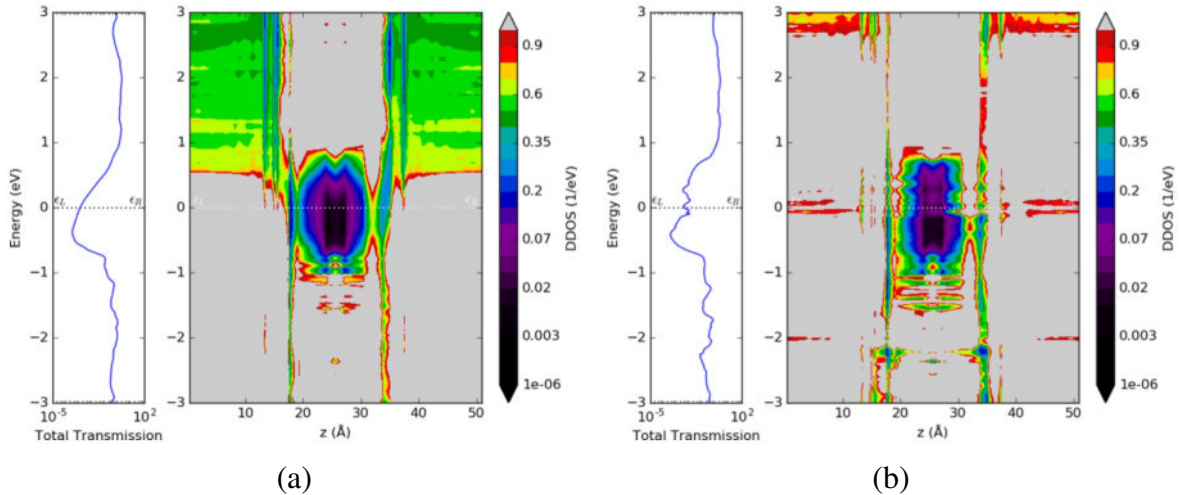
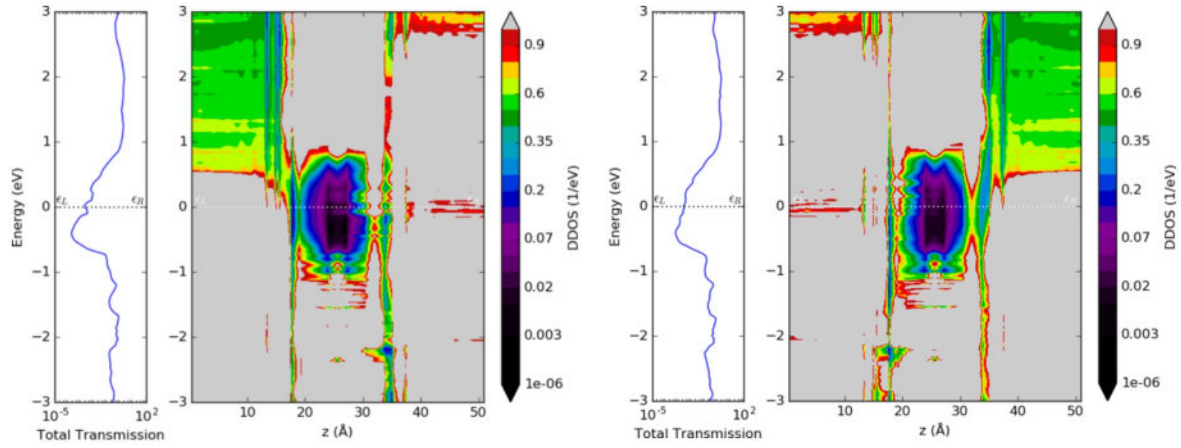


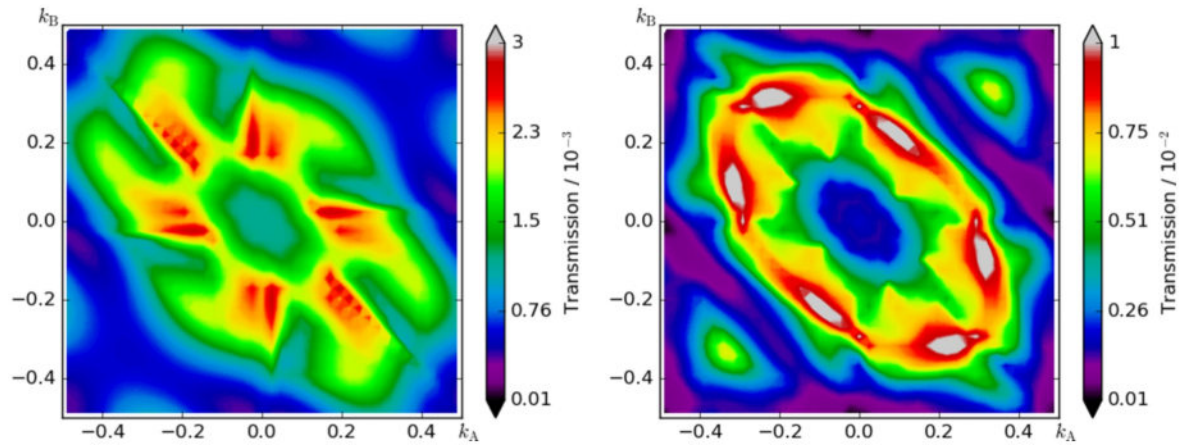
Figure 37 PLDOS for spin-up (a) and spin-down (b) channel $\text{Fe}(111)/\text{MoS}_2(3\text{-layer})/\text{Fe}(111)$ junction in parallel orientation of electrodes.



(a)

(b)

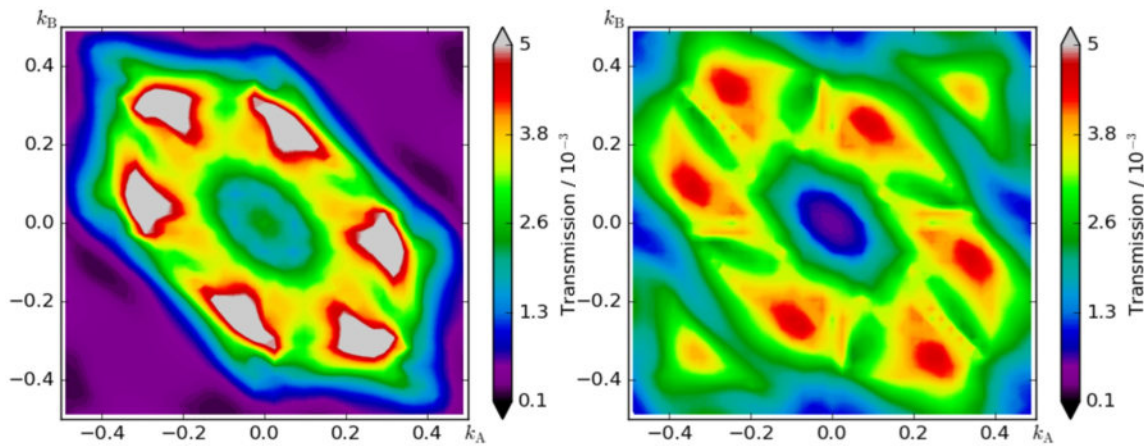
Figure 38 PLDOS for spin-up (a) and spin-down (b) channel $Fe(111)/MoS_2(3\text{-layer})/Fe(111)$ junction in the anti-parallel orientation of electrodes.



(a)

(b)

Figure 39 K -resolved transmission spectrum in spin-up (a) and spin-down (b) channel for $Fe(111)/MoS_2(3\text{-layer})/Fe(111)$ junction in parallel orientation of electrodes.



(a)

(b)

Figure 40 *K*-resolved transmission spectrum in spin-up (a) and spin-down (b) channel for Fe(111)/MoS₂(3-layer)/Fe(111) junction in the anti-parallel orientation of electrodes.

The *K*-resolved transmission spectrum for the Fe(111)/MoS₂(3-layer)/Fe(111) junction at zero-bias in the P and AP orientation of electrodes is shown in Figure 39 and Figure 40. In the P orientation of the electrodes, the 2D colour map for spin-up shows six points in the 2D Brillouin zone contributing to the order of 2.6×10^{-3} and for spin-down channel, six points in the 2D Brillouin zone contributing to the order of 10^{-2} to the total transmission at the Fermi level. The transmission for the spin-down is higher due to the spin-down channel crossing the Fermi level. For the AP orientation of electrodes, the 2D colour map shows the transmission for spin-up and spin-down channels is a combination of transmission of both the channels and six points in the 2D Brillouin zone contributing of the order of 5×10^{-3} towards the total transmission at the fermi level under zero-bias condition.

Fe(111)/MoS₂(5-layer)/Fe(111) junction

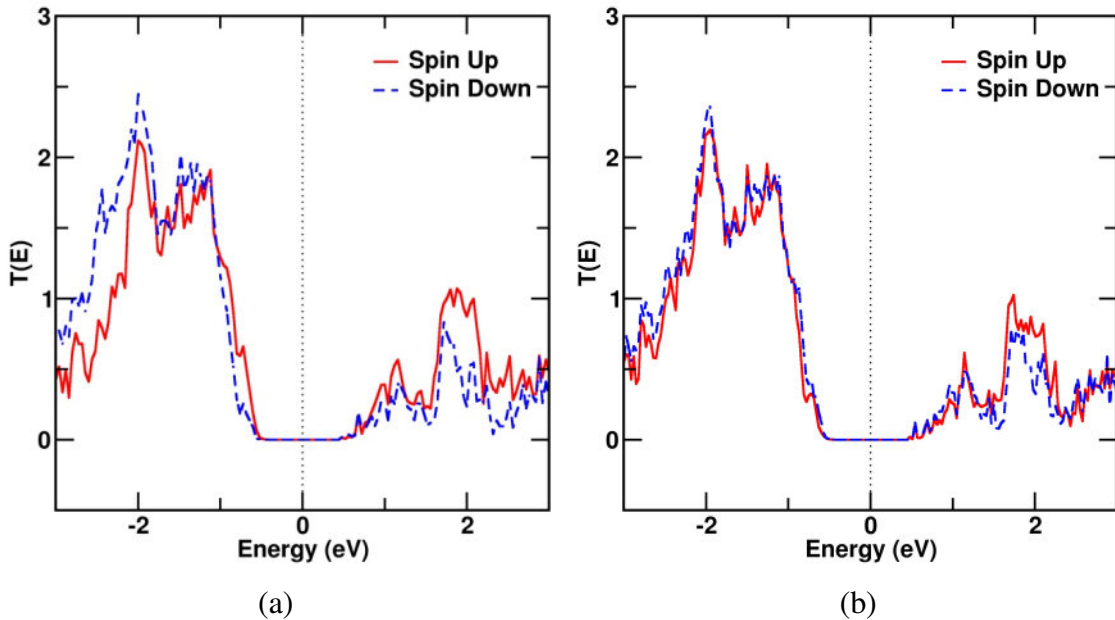


Figure 41 *Transmission spectrum for Fe(111)/MoS₂(5-layer)/Fe(111) junction in parallel (a) and anti-parallel (b) orientation of electrodes.*

The transmission spectrum for the Fe(111)/MoS₂(5-layer)/Fe(111) junction in P and AP orientation of electrodes under zero-bias conditions is shown in Figure 41. For the P, the

transmission at the Fermi level is of the order of 3×10^{-6} for both spin-up and channel and AP, and the transmission spectrum at the Fermi-level for both channels is the same and is of the order of 3.4×10^{-6} .

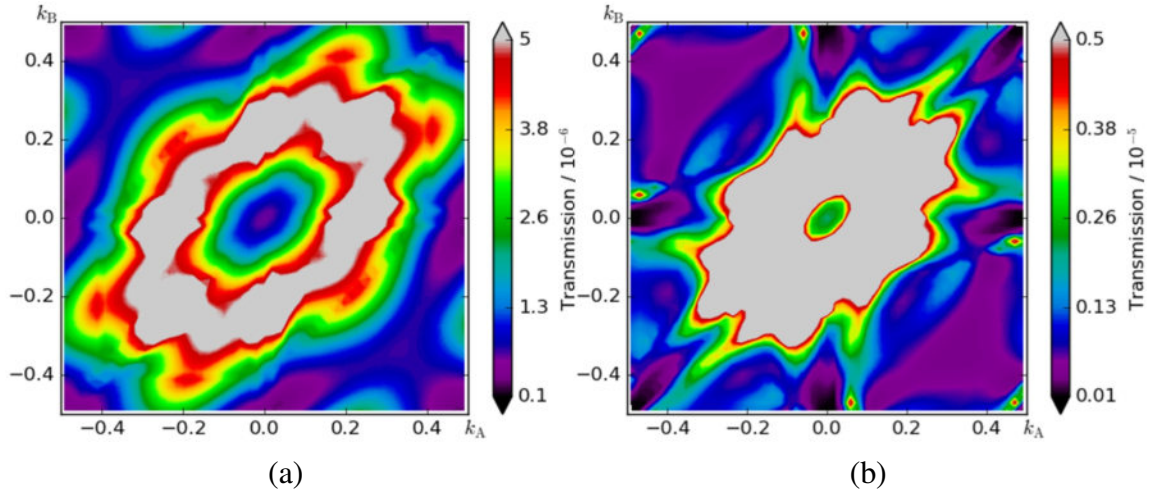


Figure 42 *K*-resolved transmission spectrum for spin-up (a) and spin-down (b) channel for $Fe(111)/MoS_2(5\text{-layer})/Fe(111)$ junction in parallel orientation of electrodes.

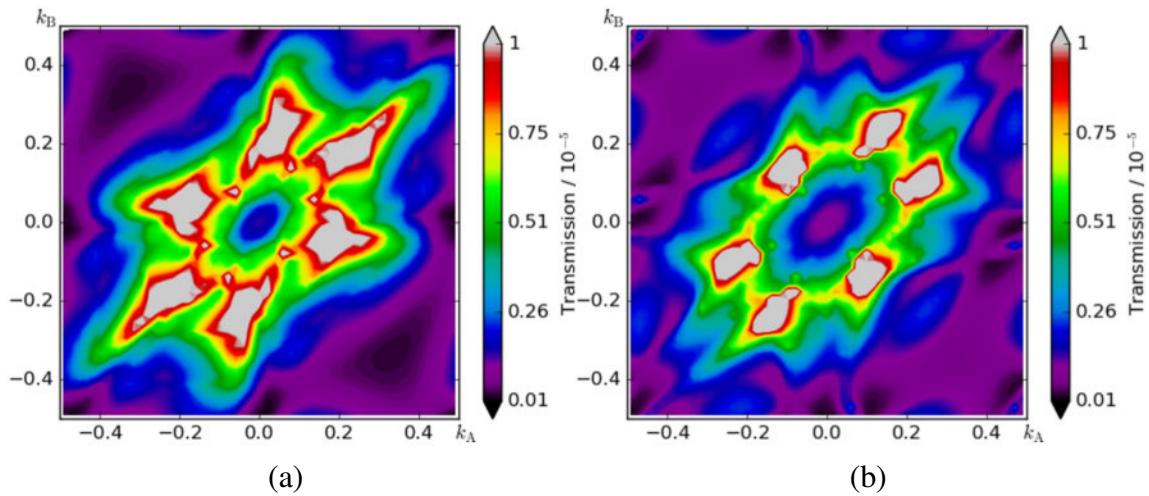


Figure 43 *K*-resolved transmission spectrum for spin-up (a) and spin-down (b) channel of $Fe(111)/MoS_2(3\text{-layer})/Fe(111)$ junction in the parallel orientation of electrodes.

The *K*-resolved transmission spectrum of spin-up and spin-down channels in the P and AP orientation of the electrodes is shown in Figure 42 and Figure 43, respectively. The 2D colour map in Figure 42 Shows that for spin-up and spin-down, a maximum contribution to the total transmission having a transmission coefficient of the order of 5×10^{-6} comes from a

region close to the Brillouin zone centre. For the AP orientation of electrodes, the 2D colour map in Figure 43 Shows that for spin-up and spin-down, six points with a transmission coefficient of the order of 1×10^{-5} contribute to the total transmission from the 2D Brillouin zone.

The PDOS of five layers of MoS₂ and the PDOS for the middle layer of MoS₂ in the five-layer MoS₂ is shown in Figure 44. From the PDOS, it's evident that the thickness of five layers of MoS₂ as the spacer is thick enough to keep the semiconductor behaviour of the middle layer of MoS₂ and to reduce the effect of the interface. The middle layer MoS₂ retains the semiconductor nature of DOS for bulk MoS₂. The PLDOS for Fe(111)/MoS₂(5-layer)/Fe(111) junction for parallel orientation of the electrodes is shown in Figure 45. The PLDOS shows that the metal-induced states are present for the first layer of MoS₂ on both sides of the interface, and the middle layer of MoS₂ keeps the semiconducting band gap nature of bulk MoS₂.

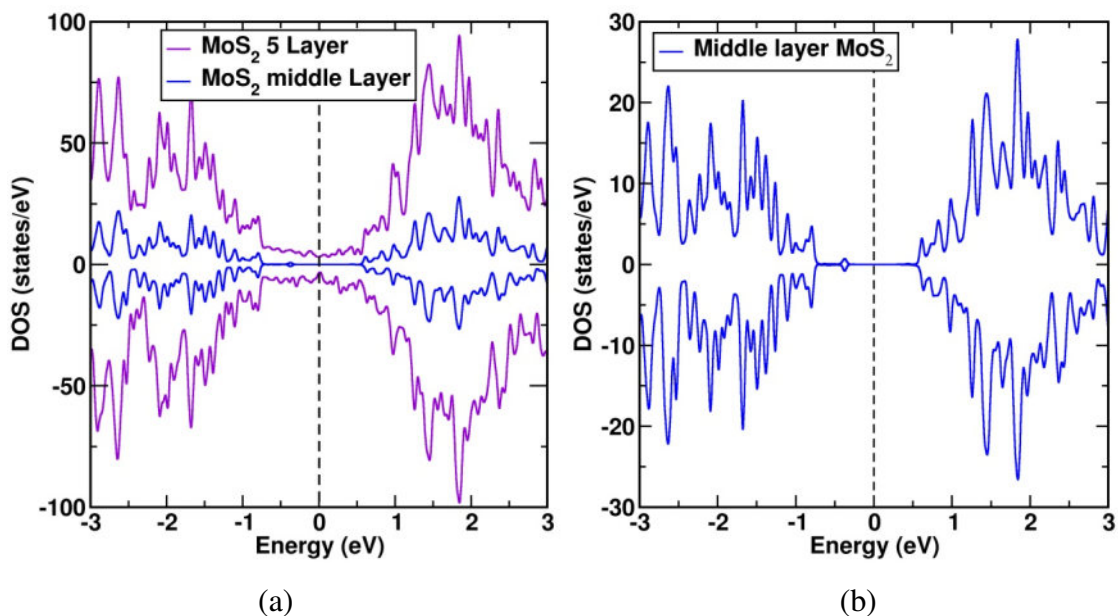


Figure 44 PDOS for 5-layer MoS₂ and the middle layer MoS₂ in the Fe(111)/MoS₂(5-layer)/Fe(111) junction

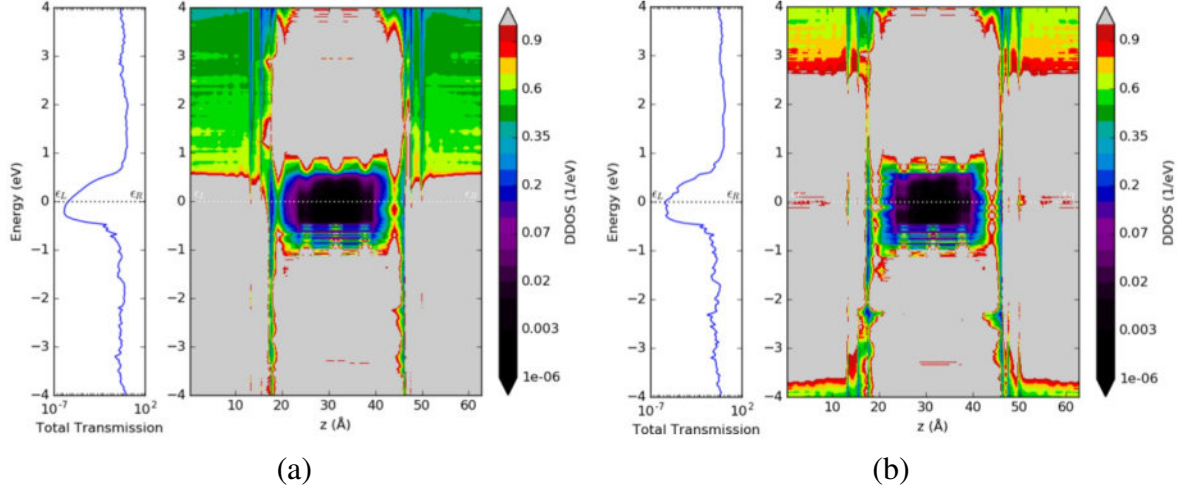


Figure 45 PLDOS for spin-up (a) and spin-down (b) channel in Fe(111)/MoS₂(5-layer)/Fe(111) junction in parallel orientation of electrodes.

Conclusion

Spin-dependent transport studies through Fe(001)/Mo_xCr_{1-x}S₂/Fe(001) junction with a thickness of three, five and seven layers of MoS₂ as spacer material and spin transport across the low strain Fe(111)/MoS₂/Fe(111) junction with a thickness of one, three and five layers of MoS₂ is studied. The Fe/MoS₂ interface with one layer and three layers of Mo_xCr_{1-x}S₂ as the spacer is metallic. The metallic nature of the interface comes from the strong coupling of Fe layers with MoS₂ layers at the interface. The strong hybridisation of Fe *d*-orbitals with *p*-orbitals of S and *d*-orbitals of Mo induces metal-induced states in the semiconducting MoS₂. The hybridisation is strong for the first layer of MoS₂ at the interface. For the next layer of MoS₂ (the second layer next to the interface), the PDOS shows only one of the spin channel crossings the fermi level, and the other spin channel has a band gap region. Thus, the second layer of MoS₂ near the interface with Fe behaves like a nearly half-metallic character. At zero-bias, the transport through a single layer of MoS₂ and Fe(111) as the electrode is high for the P orientation of electrodes, and for AP orientation, the transmission is combination of spin-up and spin-down channels of p case. In comparison to three layers of MoS₂ with Fe(001) electrode, the transmission for three-layer MoS₂ with Fe(111) as the electrode, the

transmission at zero-bias in the P orientation of electrodes has reduced by order of 10 and is 0.001 and 0.004 for spin-up and spin-down channels, respectively, for the AP orientation of electrodes, both the spin channel has a transmission of 0.002. The reduction in transmission is due to the nearly half-metallic nature of the interface MoS₂ layer and the effect of strain at the interface. For Fe(001)/Mo_xCr_{1-x}S₂/Fe(001) junctions with doping of magnetic impurity Cr in the middle layer of three, five, and seven-layer MoS₂, Cr defect levels are formed below the conduction band of doped MoS₂ layer. The addition of magnetic impurity has a improved in the spin-polarisation of the DOS for the doped MoS₂ layer. Higher doping concentration may improve the spin-polarisation of the DOS.

For a thicker junction of five layers and seven layers of MoS₂, the middle layer of five-layer MoS₂ and the middle layer and three layers of MoS₂ in the middle of the seven-layer MoS₂ keeps a semiconducting band gap and the tunneling nature of the junction is observed as the interface effect is limited to the first two layers of MoS₂ at the interface. The tunneling spin-current is higher in a 5-layer junction compared to a 7-layer junction, as with a 7-layer thick junction, the bulk behaviour of MoS₂ reappears. The 3-layer, 5-layer, and Cr-doped 7-layer devices are stable up to a bias of 0.5V. The 7-layer device is stable up to a bias of 0.7V and the stability of the junction with respect to bias voltage is related to the band gap of the spacer.

References

- [1] M. N. Baibich, J. M. Broto, A. Fert, F. N. Van Dau, F. Petroff, P. Eitenne, G. Creuzet, A. Friederich, and J. Chazelas, Giant magnetoresistance of (001)Fe/(001)Cr magnetic superlattices, *Phys Rev Lett* **61**, 2472 (1988).
- [2] G. Binasch, P. Grünberg, F. Saurenbach, and W. Zinn, Enhanced magnetoresistance in layered magnetic structures with antiferromagnetic interlayer exchange, *Phys Rev B* **39**, 4828 (1989).
- [3] M. Julliere, Tunneling between ferromagnetic films, *Phys Lett A* **54**, 225 (1975).
- [4] C. H. Tsang, R. E. Fontana, T. Lin, D. E. Heim, B. A. Gurney, and M. L. Williams, Design, fabrication, and performance of spin-valve read heads for magnetic recording applications, *IBM J Res Dev* **42**, 103 (1998).
- [5] S. A. Wolf, D. D. Awschalom, R. A. Buhrman, J. M. Daughton, S. Von Molnár, M. L. Roukes, A. Y. Chtchelkanova, and D. M. Treger, Spintronics: A spin-based electronics vision for the future, *Science* **294**, 1488 (2001).
- [6] A. Hirohata, K. Yamada, Y. Nakatani, L. Prejbeanu, B. Diény, P. Pirro, and B. Hillebrands, Review on spintronics: Principles and device applications, *J Magn Magn Mater* **509**, 166711 (2020).
- [7] I. Žutić, J. Fabian, and S. Das Sarma, Spintronics: Fundamentals and applications, *Rev. Mod. Phys.* **76**, 323 (2004).
- [8] S. A. Wolf, A. Y. Chtchelkanova, and D. M. Treger, Spintronics - A retrospective and perspective, *IBM J Res Dev* **50**, 101 (2006).
- [9] S. Tehrani et al., Magnetoresistive random access memory using magnetic tunnel junctions, *Proc. IEEE* **91**, 703 (2003).
- [10] A. V. Khvalkovskiy et al., Basic principles of STT-MRAM cell operation in memory arrays, *J Phys D Appl Phys* **46**, 074001 (2013).
- [11] C. Chappert, A. Fert, and F. N. Van Dau, The emergence of spin electronics in data storage, *Nature Materials* **6**, 813 (2007).
- [12] B. Behin-Aein, D. Datta, S. Salahuddin, and S. Datta, Proposal for an all-spin logic device with built-in memory, *Nature Nanotechnology* **5**, 266 (2010).
- [13] J. F. Dayen, S. J. Ray, O. Karis, I. J. Vera-Marun, and M. V. Kamalakar, Two-dimensional van der Waals spinterfaces and magnetic-interfaces, *Appl Phys Rev* **7**, (2020).
- [14] A. K. Geim and K. S. Novoselov, The rise of graphene, *Nat Mater* **6**, 183 (2007).
- [15] A. K. Geim and I. V. Grigorieva, Van der Waals heterostructures, *Nature* **499**, 419 (2013).
- [16] S. Z. Butler et al., Progress, challenges, and opportunities in two-dimensional materials beyond graphene, *ACS Nano* **7**, 2898 (2013).
- [17] K. S. Novoselov, A. Mishchenko, A. Carvalho, and A. H. Castro Neto, 2D materials and van der Waals heterostructures, *Science* **353**, (2016).

- [18] Y. Lei et al., Graphene and Beyond: Recent Advances in Two-Dimensional Materials Synthesis, Properties, and Devices, ACS Nanoscience Au **2**, 450 (2022).
- [19] A. H. Castro Neto, F. Guinea, N. M. R. R. Peres, K. S. Novoselov, and A. K. Geim, The electronic properties of graphene, Rev. Mod. Phys. **81**, 109 (2009).
- [20] K. S. Novoselov, A. K. Geim, S. V. Morozov, D. Jiang, M. I. Katsnelson, I. V. Grigorieva, S. V. Dubonos, and A. A. Firsov, Two-dimensional gas of massless Dirac fermions in graphene, Nature **438**, 197 (2005).
- [21] K. S. Novoselov, Z. Jiang, Y. Zhang, S. V. Morozov, H. L. Stormer, U. Zeitler, J. C. Maan, G. S. Boebinger, P. Kim, and A. K. Geim, Room-temperature quantum hall effect in graphene, Science **315**, 1379 (2007).
- [22] A. K. Geim, K. Novoselov, and P. Blake, Graphene spin valve devices, IEEE Trans Magn **42**, 2694 (2006).
- [23] Y. Zhang, Y. W. Tan, H. L. Stormer, and P. Kim, Experimental observation of the quantum Hall effect and Berry's phase in graphene, Nature **438**, 201 (2005).
- [24] D. S. L. Abergel, V. Apalkov, J. Berashevich, K. Ziegler, and T. Chakraborty, Properties of graphene: A theoretical perspective, Adv Phys **59**, 261 (2010).
- [25] H. Lv, H. Wu, J. Liu, J. Yu, J. Niu, J. Li, Q. Xu, X. Wu, and H. Qian, High carrier mobility in suspended-channel graphene field effect transistors, Appl Phys Lett **103**, (2013).
- [26] C. Berger et al., Electronic Confinement and Coherence in Patterned Epitaxial Graphene, Science **312**, 1191 (2006).
- [27] N. Tombros, C. Jozsa, M. Popinciuc, H. T. Jonkman, and B. J. Van Wees, Electronic spin transport and spin precession in single graphene layers at room temperature, Nature **448**, 571 (2007).
- [28] W. Han and R. K. Kawakami, Spin relaxation in single-layer and bilayer graphene, Phys Rev Lett **107**, (2011).
- [29] W. Han, J. R. Chen, D. Wang, K. M. McCreary, H. Wen, A. G. Swartz, J. Shi, and R. K. Kawakami, Spin relaxation in single-layer graphene with tunable mobility, Nano Lett **12**, 3443 (2012).
- [30] M. Drögeler, F. Volmer, M. Wolter, B. Terrés, K. Watanabe, T. Taniguchi, G. Güntherodt, C. Stampfer, and B. Beschoten, Nanosecond spin lifetimes in single- and few-layer graphene-hBN heterostructures at room temperature, Nano Lett **14**, 6050 (2014).
- [31] T. Y. Yang et al., Observation of long spin-relaxation times in bilayer graphene at room temperature, Phys Rev Lett **107**, 047206 (2011).
- [32] S. Das Sarma, S. Adam, E. H. Hwang, and E. Rossi, Electronic transport in two-dimensional graphene, Rev Mod Phys **83**, 407 (2011).
- [33] A. Avsar, H. Ochoa, F. Guinea, B. Zyilmaz, B. J. Van Wees, and I. J. Vera-Marun, Colloquium: Spintronics in graphene and other two-dimensional materials, Rev Mod Phys **92**, (2020).
- [34] W. Han, R. K. Kawakami, M. Gmitra, and J. Fabian, Graphene spintronics, Nature Nanotechnology **9**, 794 (2014).

- [35] P. Seneor, B. Dlubak, M. B. Martin, A. Anane, H. Jaffres, and A. Fert, Spintronics with graphene, *MRS Bull* **37**, 1245 (2012).
- [36] S. Roche et al., Graphene spintronics: the European Flagship perspective, *2d Mater* **2**, 030202 (2015).
- [37] B. Radisavljevic, A. Radenovic, J. Brivio, V. Giacometti, and A. Kis, Single-layer MoS₂ transistors, *Nat Nanotechnol* **6**, 147 (2011).
- [38] X. Qian, J. Liu, L. Fu, and J. Li, Quantum spin hall effect in two - Dimensional transition metal dichalcogenides, *Science* **346**, 1344 (2014).
- [39] N. Singh, G. Jabbour, and U. Schwingenschlögl, Optical and photocatalytic properties of two-dimensional MoS₂, *Eur Phys J B* **85**, 392 (2012).
- [40] Z. Y. Zhu, Y. C. Cheng, and U. Schwingenschlögl, Giant spin-orbit-induced spin splitting in two-dimensional transition-metal dichalcogenide semiconductors, *Phys Rev B Condens Matter Phys* **84**, 1 (2011).
- [41] N. Zibouche, A. Kuc, J. Musfeldt, and T. Heine, Transition-metal dichalcogenides for spintronic applications, *Ann Phys* **526**, 395 (2014).
- [42] L. Sun et al., Spin-orbit splitting in single-layer MoS₂ revealed by triply resonant raman scattering, *Phys Rev Lett* **111**, 126801 (2013).
- [43] K. F. Mak, K. He, J. Shan, and T. F. Heinz, Control of valley polarization in monolayer MoS₂ by optical helicity, *Nature Nanotechnology* **7**, 494 (2012).
- [44] H. Zeng, J. Dai, W. Yao, D. Xiao, and X. Cui, Valley polarization in MoS₂ monolayers by optical pumping, *Nature Nanotechnology* **7**, 490 (2012).
- [45] J. R. Schaibley, H. Yu, G. Clark, P. Rivera, J. S. Ross, K. L. Seyler, W. Yao, and X. Xu, Valleytronics in 2D materials, *Nature Reviews Materials* **1**, 11 (2016).
- [46] S. V. Morozov, K. S. Novoselov, M. I. Katsnelson, F. Schedin, D. C. Elias, J. A. Jaszczak, and A. K. Geim, Giant intrinsic carrier mobilities in graphene and its bilayer, *Phys Rev Lett* **100**, 016602 (2008).
- [47] D. Xiao, G. Bin Liu, W. Feng, X. Xu, and W. Yao, Coupled spin and valley physics in monolayers of MoS₂ and other group-VI dichalcogenides, *Phys Rev Lett* **108**, 1 (2012).
- [48] Y. C. Cheng, Q. Y. Zhang, and U. Schwingenschlögl, Valley polarization in magnetically doped single-layer transition-metal dichalcogenides, *Phys Rev B Condens Matter Phys* **89**, (2014).
- [49] S. Wu et al., Electrical tuning of valley magnetic moment through symmetry control in bilayer MoS₂, *Nature Physics* **9**, 149 (2013).
- [50] A. Fert, Nobel lecture: Origin, development, and future of spintronics, *Rev Mod Phys* **80**, 1517 (2008).
- [51] S. D. Bader and S. S. P. Parkin, Spintronics, *Annu Rev Condens Matter Phys* **1**, 71 (2010).
- [52] L. F. Mattheiss, Band structures of transition-metal-dichalcogenide layer compounds, *Phys Rev B* **8**, 3719 (1973).

- [53] R. Coehoorn, C. Haas, J. Dijkstra, C. J. F. Flipse, R. A. De Groot, and A. Wold, Electronic structure of MoSe₂, MoS₂, and WSe₂. I. Band-structure calculations and photoelectron spectroscopy, *Phys Rev B* **35**, 6195 (1987).
- [54] A. Splendiani, L. Sun, Y. Zhang, T. Li, J. Kim, C. Y. Chim, G. Galli, and F. Wang, Emerging photoluminescence in monolayer MoS₂, *Nano Lett* **10**, 1271 (2010).
- [55] J. K. Ellis, M. J. Lucero, and G. E. Scuseria, The indirect to direct band gap transition in multilayered MoS₂ as predicted by screened hybrid density functional theory, *Appl Phys Lett* **99**, (2011).
- [56] K. Dolui, A. Narayan, I. Rungger, and S. Sanvito, Efficient spin injection and giant magnetoresistance in Fe/MoS₂/Fe junctions, *Phys Rev B Condens Matter Phys* **90**, 1 (2014).
- [57] H. C. Wu et al., Spin-dependent transport properties of Fe₃O₄/MoS₂/Fe₃O₄ junctions, *Sci Rep* **5**, 1 (2015).
- [58] W. Wang et al., Spin-Valve Effect in NiFe/MoS₂/NiFe Junctions, *Nano Lett* **15**, 5261 (2015).
- [59] B. Canto, C. P. Gouvea, B. S. Archanjo, J. E. Schmidt, and D. L. Baptista, On the Structural and Chemical Characteristics of Co/Al₂O₃/graphene Interfaces for Graphene Spintronic Devices, *Scientific Reports* **5**, 1 (2015).
- [60] J. Y. Chen, Y. C. Lau, J. M. D. Coey, M. Li, and J. P. Wang, High Performance MgO-barrier Magnetic Tunnel Junctions for Flexible and Wearable Spintronic Applications, *Scientific Reports* **7**, 1 (2017).
- [61] B. Taudul et al., Tunneling Spintronics across MgO Driven by Double Oxygen Vacancies, *Adv Electron Mater* **3**, 1600390 (2017).
- [62] M. Schäfers, V. Drewello, G. Reiss, A. Thomas, K. Thiel, G. Eilers, M. Münzenberg, H. Schuhmann, and M. Seibt, Electric breakdown in ultrathin MgO tunnel barrier junctions for spin-transfer torque switching, *Appl Phys Lett* **95**, (2009).
- [63] K. Tarawneh, N. Al-Aqtash, and R. Sabirianov, Large magnetoresistance in planar Fe/MoS₂/Fe tunnel junction, *Comput Mater Sci* **124**, 15 (2016).
- [64] W. Rotjanapittayakul, W. Pijitrojana, T. Archer, S. Sanvito, and J. Prasongkit, Spin injection and magnetoresistance in MoS₂-based tunnel junctions using Fe₃Si Heusler alloy electrodes, *Sci Rep* **8**, 1 (2018).
- [65] M. Y. Yin, X. C. Wang, W. B. Mi, and B. H. Yang, First principles prediction on the interfaces of Fe/MoS₂, Co/MoS₂ and Fe₃O₄/MoS₂, *Comput Mater Sci* **99**, 326 (2015).
- [66] G. Schmidt, D. Ferrand, L. Molenkamp, A. Filip, and B. van Wees, Fundamental obstacle for electrical spin injection from a ferromagnetic metal into a diffusive semiconductor, *Phys Rev B* **62**, R4790 (2000).
- [67] J. M. De Teresa, A. Barthélémy, A. Fert, J. P. Contour, F. Montaigne, and P. Seneor, Role of Metal-Oxide Interface in Determining the Spin Polarization of Magnetic Tunnel Junctions, *Science* **286**, 507 (1999).
- [68] E. Y. Tsymbal, O. N. Mryasov, and P. R. LeClair, Spin-dependent tunnelling in magnetic tunnel junctions, *Journal of Physics: Condensed Matter* **15**, R109 (2003).

- [69] S. Smidstrup et al., QuantumATK: An integrated platform of electronic and atomic-scale modelling tools, *J. Phys: Condens. Matter* **32**, 15901 (2020).
- [70] M. Brandbyge, J. L. Mozos, P. Ordejón, J. Taylor, and K. Stokbro, Density-functional method for nonequilibrium electron transport, *Phys Rev B Condens Matter Phys* **65**, 1654011 (2002).
- [71] D. Stradi, U. Martinez, A. Blom, M. Brandbyge, and K. Stokbro, General atomistic approach for modeling metal-semiconductor interfaces using density functional theory and nonequilibrium Green's function, *Phys Rev B* **93**, 28 (2016).
- [72] D. M. Ceperley and B. J. Alder, Ground State of the Electron Gas by a Stochastic Method, *Phys Rev Lett* **45**, 566 (1980).
- [73] S. Smidstrup, D. Stradi, J. Wellendorff, P. A. Khomyakov, U. G. Vej-Hansen, M.-E. Lee, T. Ghosh, E. Jónsson, H. Jónsson, and K. Stokbro, First-principles Green's-function method for surface calculations: A pseudopotential localized basis set approach, *Phys Rev B* **96**, 195309 (2017).
- [74] J. M. Soler, E. Artacho, J. D. Gale, A. García, J. Junquera, P. Ordejón, and D. Sánchez-Portal, The SIESTA method for ab initio order-N materials simulation, *Journal of Physics: Condensed Matter* **14**, 2745 (2002).
- [75] D. Stradi, L. Jelver, S. Smidstrup, and K. Stokbro, Method for determining optimal supercell representation of interfaces, *Journal of Physics: Condensed Matter* **29**, 185901 (2017).
- [76] H. J. Monkhorst and J. D. Pack, Special points for Brillouin-zone integrations, *Phys Rev B* **13**, 5188 (1976).
- [77] C. Huang, Y. Jin, W. Wang, L. Tang, C. Song, and F. Xiu, Manganese and chromium doping in atomically thin MoS₂, *Journal of Semiconductors* **38**, (2017).
- [78] A. R. Sahoo and S. Chandra, An investigation on electronic and magnetic properties of Cr substituted MoS₂ monolayer and multilayers—hybrid functional calculations, *Sādhanā* **49**, 103 (2024).